

Nuclear spin diffusion in the central spin system of a GaAs/AlGaAs quantum dot

Peter Millington-Hotze and Evgeny A. Chekhovich*

Department of Physics and Astronomy, University of Sheffield, Sheffield S3 7RH, United Kingdom

Santanu Manna, Saimon F. Covre da Silva, and Armando Rastelli

Institute of Semiconductor and Solid State Physics,

Johannes Kepler University Linz, Altenbergerstr. 69, 4040 Linz, Austria

(Dated: August 4, 2022)

The spin diffusion concept provides a classical description of a purely quantum-mechanical evolution in inhomogeneously polarized many-body systems such as nuclear spin lattices. The central spin of a localized electron alters nuclear spin diffusion in a way that is still poorly understood. In contrast to previous predictions, we show experimentally that in GaAs/AlGaAs quantum dots the electron spin accelerates nuclear spin diffusion, without forming any Knight field gradient barrier. Such acceleration is present even at high magnetic fields, which we explain as a result of electron spin-flip fluctuations. Diffusion-limited nuclear spin lifetimes range between 1 and 10 s, providing plenty of room for recent proposals seeking to store and process quantum information using quantum dot nuclear spins.

I. INTRODUCTION

Interacting many-body spin ensembles exhibit a variety of phenomena such as phase transitions [1, 2] spin waves [3, 4] and emergent thermodynamics [5, 6]. Spin diffusion [7, 8] is one of the earliest studied phenomena, where unitary quantum-mechanical evolution results in an irreversible dissipation of a localized spin polarization that is well described by the classical diffusion model. Pure spin diffusion in homogeneous solids has been observed in a few notable examples [9, 10]. However, most systems of interest are inhomogeneous by nature. In particular, magnetic (hyperfine) interaction with the central spin of a localized electron [Fig. 1(a)] causes shifts (known as the Knight shifts [11, 12]) in the nuclear spin energy levels [Fig. 1(b)]. The resulting nuclear spin dynamics are complicated, as observed in a wide range of solid state impurities [13–19] and semiconductor nanostructures [17, 20–25]. It is still an open question whether the inhomogeneous Knight shifts accelerate [23, 26, 27] or suppress [16, 25, 27–30] spin diffusion between the nuclei. Resolving this

* e.chekhovich@sheffield.ac.uk

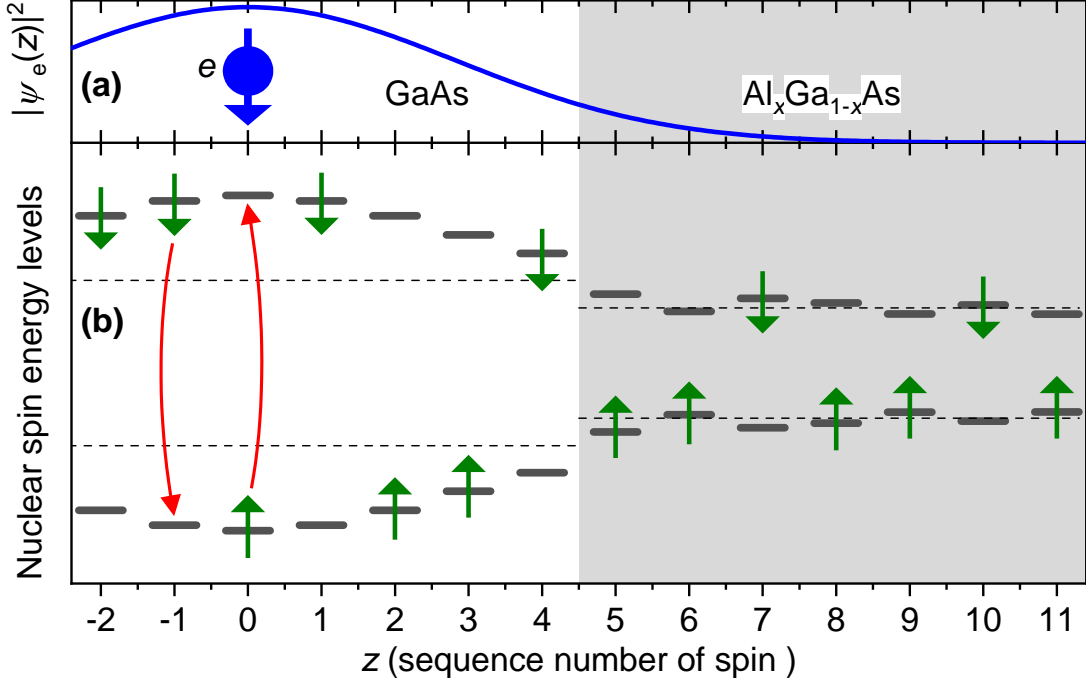


FIG. 1. Schematic of a central spin model, sketched for the one-dimensional case, along the growth axis z of a GaAs/AlGaAs structure. (a) Wavefunction density $|\psi_e|^2$ of an electron (e , ball and arrow) localized in GaAs. (b) Energy levels of the nuclei, that are depicted for simplicity as spins $1/2$, and can occupy states with $+1/2$ and $-1/2$ spin projections (up and down arrows). Dashed lines show the bulk nuclear spin energies dominated by the external magnetic field B_z . These bulk energies are generally different in GaAs ($z \leq 4$) and AlGaAs ($z \geq 5$) due to the difference in chemical shifts and homogeneous strain. The energies of the individual nuclei are further shifted by the electron Knight field (mainly in GaAs) and by the atomic-scale strain disorder in the AlGaAs alloy. Magnetic dipole interaction between the nuclei can result in spin exchange via a flip-flop process, sketched by the curved arrows for nuclei at $z = -1$ and $z = 0$ as an example. If energy mismatch is larger than the nuclear spin level homogenous broadening, for example for nuclei at $z = 4$ and $z = 5$, spin exchange becomes prohibited, suppressing nuclear spin diffusion.

dilemma is both of fundamental interest and practical importance for the recent proposals to use nuclear spins as quantum memories and registers [31–33], since spin diffusion would set an ultimate limit to the longevity of any useful quantum state.

Figure 1 sketches the central spin model where an electron can be trapped in a GaAs layer surrounded by the AlGaAs barriers, and for simplicity spin- $1/2$ particles are used to describe the energy levels of the nuclei subject to the strong external magnetic field B_z . Any two nuclear spins i and j are coupled by the dipole-dipole interaction $\propto 2\hat{I}_{z,i}\hat{I}_{z,j} - (\hat{I}_{x,i}\hat{I}_{x,j} + \hat{I}_{y,i}\hat{I}_{y,j})$, where $\hat{I}_{x,i}$, $\hat{I}_{y,i}$ and $\hat{I}_{z,i}$ are the Cartesian components of the spin operator \mathbf{I}_i of the i -th nucleus. The last two

terms of the dipole-dipole interaction describe a flip-flop spin exchange process (dashed arrows at $z = -1$ and 0 in Fig. 1(b)), responsible for the transfer of spin polarization in space, known as spin diffusion. The electric quadrupolar moments of the spin-3/2 nuclei make them sensitive to electric field gradients (EFGs), which can be induced by the GaAs/AlGaAs interfaces roughness ($z = 4.5$) or atomic-scale strains arising from random positioning of the aluminium atoms [34, 35] in AlGaAs ($z \geq 5$). The resulting energy splitting mismatch between the adjacent nuclei can impede nuclear spin diffusion.

When an electron is added, its spin \mathbf{s} couples to the nuclear spin ensemble via hyperfine interaction:

$$\hat{\mathcal{H}}_{\text{hf}} = \sum_j A_j (\hat{s}_x \hat{I}_{x,j} + \hat{s}_y \hat{I}_{y,j} + \hat{s}_z \hat{I}_{z,j}), \quad (1)$$

where the summation goes over all nuclei j , and the coupling constants A_j are proportional to the electron density $|\psi_e(\mathbf{r}_j)|^2$ at the nuclear sites \mathbf{r}_j . On the one hand, through the term $\hat{s}_z \hat{I}_z$, the electron spin can produce a further diffusion barrier [16, 25, 27–30], at the points of strong Knight shift gradient ($z = 3$ in Fig. 1(a)). On the other hand, the electron spin can mediate spin flip-flops between two distant nuclei with similar energy splitting (e.g. $z = -2$ and $z = 2$), potentially opening a new channel for spin diffusion, especially at low magnetic fields [23, 26, 27].

Here, we examine electron-controlled nuclear spin diffusion in high quality epitaxial GaAs/AlGaAs quantum dots (QDs), which emerged recently as an excellent platform for quantum light emitters [36–38] as well as spin qubits [33, 39] and quantum memories [32]. Crucially, we design experiments where nuclear spin dynamics are examined either in absence or in presence of the electron central spin, but under otherwise identical initial nuclear spin state. In this way, we distinguish with high accuracy the effects specific to the electron spin, and demonstrate that no observable Knight field barrier is formed. Instead, the nuclear-nuclear interactions mediated by the electron spin accelerate nuclear spin diffusion up to unexpectedly high magnetic fields – we attribute this to the previously neglected impact of the electron spin flips. Our results answer a long-standing question in spin physics, and provide practical guidelines for the design and optimization of quantum dot electron-nuclear spin qubits and quantum memories.

II. SAMPLE AND EXPERIMENTAL TECHNIQUES

The studied heterostructure is grown by in-situ etching of nanoholes [41, 42] in the AlGaAs surface [Figs. 2(a,b)], which are then infilled with GaAs to form the quantum dots (QDs). The

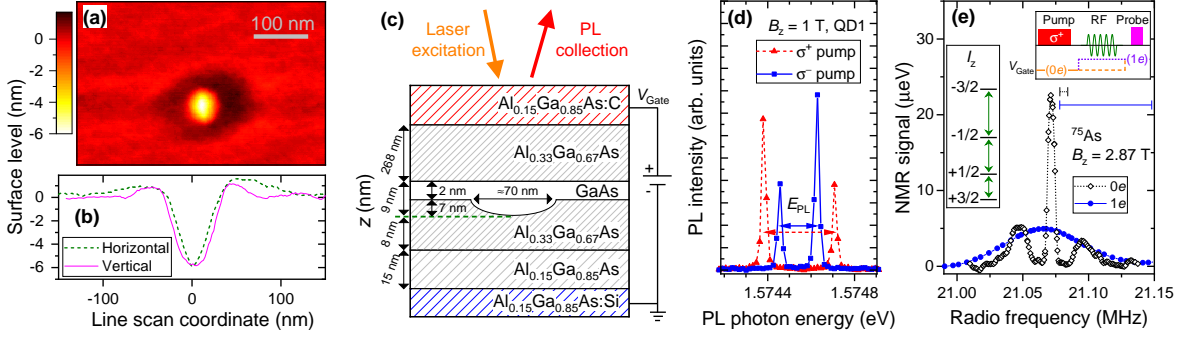


FIG. 2. (a) Atomic force microscopy (AFM) profile of the AlGaAs surface after nanohole etching. (b) Surface level profiles taken along the horizontal and vertical lines through the center of the nanohole in (a). (c) Schematic (not to scale) of the sample structure. GaAs quantum dots (QDs) are formed by infilling of the in-situ etched nanoholes in the bottom $\text{Al}_{0.33}\text{Ga}_{0.67}\text{As}$ barrier. The bottom (top) $\text{Al}_{0.15}\text{Ga}_{0.85}\text{As}$ layer is n (p) type doped to form a $p-i-n$ diode structure. External gate bias V_{Gate} is applied for deterministic QD charging with electrons. (d) Photoluminescence (PL) spectra of a negatively charged trion X^- following σ^+ (triangles) and σ^- optical pumping which induces nuclear spin polarization that manifests in hyperfine shifts of the Zeeman doublet spectral splitting ΔE_{PL} . (e) Optically detected NMR of the ^{75}As spin-3/2 nuclei measured in a single QD. Strain-induced quadrupolar shifts of the nuclear spin-3/2 levels (left inset) give rise to an NMR triplet with splitting $\nu_{\text{Q}} \approx 24$ kHz, observed in an empty QD ($0e$, diamonds). Charging the QD with a single electron ($1e$, circles) induces inhomogeneous Knight shifts observed as NMR spectral broadening. The measurement is conducted using “inverse NMR” signal amplification technique [40], with spectral resolution shown by the horizontal bars (smaller for $0e$ and larger for $1e$). The measurement pump-probe cycle is shown in the top inset. The bias V_{Gate} is tuned to $0e$ charge state for optical pumping of the nuclear spins and to $1e$ state for their optical probing. The radio frequency (RF) pulse is applied in the dark under either $0e$ or $1e$ bias.

structure is processed into a $p-i-n$ diode [Fig. 2(c)] where an external bias V_{Gate} is applied to charge QDs deterministically with individual electrons (See details in Supplementary Section 1). In this way, it is possible to study nuclear spin dynamics in an empty ($0e$) or single-electron ($1e$) state. A static magnetic field B_z is applied along the growth axis z (Faraday geometry) and the sample is kept at liquid helium temperature of 4.2 K. We use confocal microscopy configuration where QD photoluminescence (PL) is excited and collected through an aspheric lens with a focal distance of 1.45 mm and numerical aperture of 0.58. The collected PL is dispersed in a two-stage grating spectrometer, and recorded with a charge-coupled device (CCD) camera.

The changes in the PL spectral splitting ΔE_{PL} of a negatively charged trion X^- [see Fig. 2(d)] is the hyperfine shift E_{hf} , which gives a measure of an average nuclear spin polarization degree within the QD [12]. The hyperfine shifts (also known as Overhauser shifts) arise from the $\hat{s}_z \hat{I}_z$ term

of the hyperfine interaction Hamiltonian (Eq. 1). Large nonequilibrium nuclear spin polarization is generated on demand by exciting the QD with a circularly polarized pump laser, which repeatedly injects spin-polarized electrons into a QD, and causes nuclear spin polarization build up via electron-nuclear spin flip-flops described by the $\hat{s}_x\hat{I}_x + \hat{s}_y\hat{I}_y$ part of Eq. 1. A small copper wire coil is placed near the sample to produce radiofrequency (RF) oscillating magnetic field perpendicular to the static magnetic field. Application of the RF field allows for the energy spectrum of the nuclear spins to be probed via nuclear magnetic resonance (NMR). Moreover, the RF field can be used to depolarize the nuclear spins on-demand. Further details can be found in the Supplementary Section 2, including sample growth details, PL spectra, characterization of QD charge state control, and additional results at an elevated temperature of 15.2 K.

III. EXPERIMENTAL RESULTS AND DISCUSSION

A. Nuclear spin system of a GaAs quantum dot

Figure 2(e) shows NMR spectra of ^{75}As in a single GaAs QD, measured using “inverse NMR” technique with an optical Pump-RF-Probe cycle shown in the top inset. For an empty QD (open symbols), an NMR triplet is observed [43], corresponding to the three magnetic-dipole transitions between the four Zeeman-split states $I_z = \{-3/2, -1/2, +1/2, +3/2\}$ of a spin-3/2 nucleus (left inset). The central resolution-limited peak originates from the $-1/2 \leftrightarrow +1/2$ NMR transition that is weakly affected by strain. The two satellite transition peaks $\pm 1/2 \leftrightarrow \pm 3/2$ are split from the central transition peak by the strain-induced EFGs. The average splitting $\nu_Q \approx 24$ kHz between the triplet components corresponds to an average elastic strain of $\approx 2.6 \times 10^{-4}$ (Refs. [44, 45]). The satellite transitions are inhomogeneously broadened, with non-zero NMR amplitudes detected approximately in a range of $\nu_Q \in [10, 50]$ kHz, indicating that elastic strain varies within the nanoscale volume of the QD.

When a single electron occupies the QD, it induces inhomogeneous Knight shifts that exceed the quadrupolar shifts, leading to a broadened NMR peak [solid symbols in Fig. 2(e)]. From the NMR peak width, the Knight shifts, characterizing the typical coupling strength between the electron spin and an individual nuclear spin, are estimated to be $A_j/h \approx 50$ kHz, where h is the Planck’s constant.

These NMR characterization results indicate a complex interplay of dipolar, quadrupolar and hyperfine interactions governing the nuclear spin dynamics, which we now investigate experimen-

tally.

B. Nuclear spin relaxation in a GaAs quantum dot

In the nuclear spin relaxation (NSR) experiment [see timing diagram in Fig. 3(a)] any remnant nuclear spin polarization is first erased by saturating the ^{75}As , ^{69}Ga and ^{71}Ga NMR resonances in the entire heterostructure [46]. This is followed by a variable-duration (T_{Pump}) optical pumping [15, 17, 20, 22] with photon energies below the AlGaAs barrier bandgap, which prepares nuclear spin polarization localized around the QD nanoscale volume. After the pump laser is turned off, the gate bias V_{Gate} is set to a desired level for a dark time T_{Dark} – this way evolution under $0e$ or $1e$ QD charge state is studied for nominally identical initial nuclear spin polarizations. Finally, the remaining polarization within the QD volume is probed through an optically detected hyperfine shift E_{hf} .

Figure 3(b) shows the average QD nuclear spin polarization as a function of the pump-probe delay T_{Dark} during which the sample is kept in the dark. The decay is non-exponential, thus we characterize the NSR timescale $T_{1,N}$ by the half-life time over which the QD hyperfine shift E_{hf} decays to $1/2$ of its initial value. The NSR rate is then defined as $\Gamma_N = 1/T_{1,N}$. When the pumping time T_{Pump} is increased, $T_{1,N}$ notably increases, as can be seen in Figs. 3(c,d). Such dependence of $T_{1,N}$ on T_{Pump} is observed both in an empty ($0e$) and charged ($1e$) QD states, and in a wide range of magnetic fields.

C. Nuclear spin diffusion

In order to explain the results of Fig. 3, we note that nuclear spin dipole-dipole interactions conserve the nuclear spin polarization for any magnetic field exceeding the dipolar local field, typically $\lesssim 1$ mT. Therefore, at high magnetic field the decay of nuclear spin polarization can proceed via two routes: either via spin-conserving diffusion to the surrounding nuclei, or spin transfer to external degrees of freedom, including quadrupolar coupling to lattice vibrations [16, 47] or a hyperfine interaction with a charge spin [16, 48–50] that is in turn coupled to the lattice or other charges. Spin diffusion can only take place if the spatial profile of the initial nuclear spin polarization is inhomogeneous. By contrast, direct spin-lattice and hyperfine interactions have no explicit dependence on the spin polarization spatial profile. Optical pumping that is short compared to spin diffusion timescales creates nuclear spin polarization localized to the QD volume and the

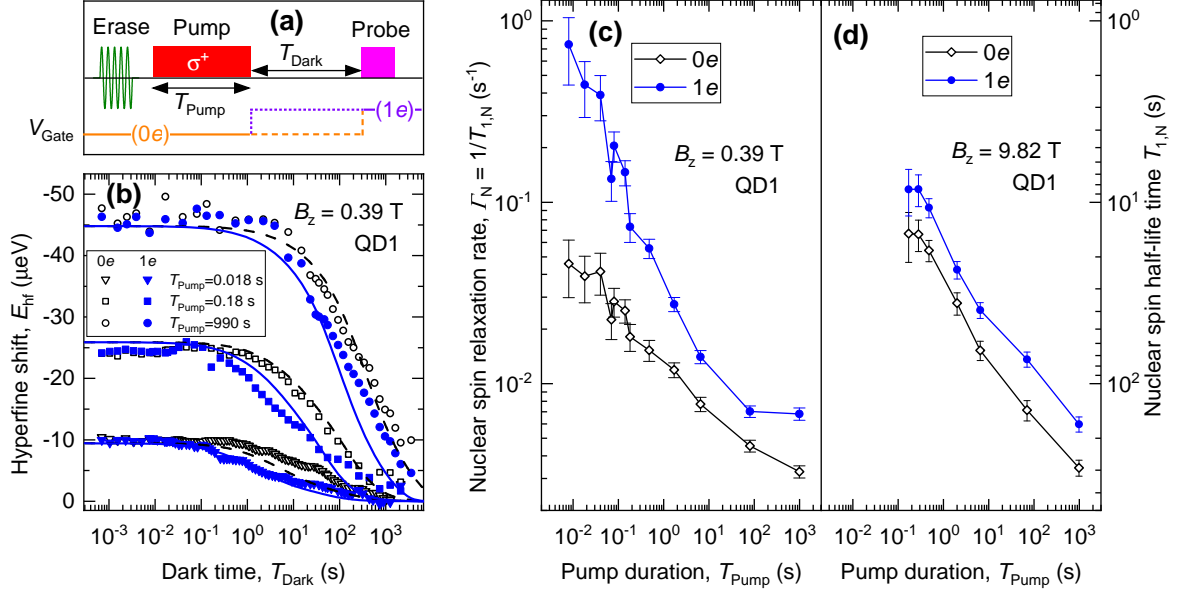


FIG. 3. (a) NSR measurement cycle starting with a radio frequency erase pulse, followed by circularly polarized (σ^+) optical pumping and then optical probing of the QD nuclear spin polarization after dark evolution delay T_{Dark} (see details in Supplementary Section 2). The sample gate bias V_{Gate} is varied allowing to choose between $0e$ (dashed line) and $1e$ (dotted line) QD charge state during T_{Dark} . (b) Dark time dependence of the hyperfine shift E_{hf} , which probes the average polarization of $\approx 10^5$ QD nuclear spins, weighted by the QD electron density $|\psi_e|^2$. The nuclear spin decay is measured (symbols) at $B_z = 0.39$ T for different pumping times T_{Pump} while keeping the QD empty ($0e$, open symbols) or charged with one electron ($1e$, solid symbols) during the dark time. Lines show numerical solution of the spin diffusion Eq. 2. (c) Fitted QD nuclear spin half-life times $T_{1,N}$ (right scale) and the corresponding NSR rates $\Gamma_N = 1/T_{1,N}$ (left scale) at magnetic field $B_z = 0.39$ T. (d) same as (c) for $B_z = 9.82$ T. All results are for the same individual dot QD1. Error bars are 95% confidence intervals.

resulting short $T_{1,N}$ is therefore a clear indicator of spin diffusion as the dominant NSR mechanism [15, 17, 20, 22]. Conversely, long pumping provides enough time for nuclear polarization to diffuse from the QD into the surrounding AlGaAs barriers, suppressing any subsequent spin diffusion out of the QD and increasing $T_{1,N}$, as observed in Figs. 3(c,d).

In order to complement our experimental investigation we model the spatiotemporal evolution of the nuclear spin polarization degree $P_N(t, z)$ by solving numerically the one dimensional spin diffusion equation

$$\frac{\partial P_N(t, z)}{\partial t} = D(t) \frac{\partial^2 P_N(t, z)}{\partial z^2} + w(t) |\psi_e(z)|^2 (P_{N,0} - P_N(t, z)), \quad (2)$$

where the last term describes optical nuclear spin pumping with a rate proportional to electron density $|\psi_e(z)|^2$ and the time-dependent factor $w(t)$ equal to 0 or w_0 when optical pumping is off or on, respectively. Correspondingly, the spin diffusion coefficient $D(t)$ takes two discrete values D_{Dark} or D_{Pump} when optical pumping is off or on, respectively. $P_{N,0}$ is a steady state nuclear spin polarization degree that optical pumping would generate in the absence of spin diffusion. Eq. 2 is solved numerically and the parameters such as $D_{\text{Dark}}^{(ne)}$, $w_0(B_z)$, $D_{\text{Pump}}(B_z)$ are varied to achieve the best fit to the entire experimental datasets of $E_{\text{hf}}(T_{\text{Pump}}, T_{\text{Dark}})$ measured at $B_z = 0.39, 9.82$ T for empty ($n = 0$) and charged ($n = 1$) QD states. The best-fit calculated dynamics are shown by the lines in Fig. 3(b) and capture well the main features of the experimentally measured nuclear spin decay, confirming the validity of the spin diffusion picture. The one-dimensional character of diffusion, occurring predominantly along the sample growth z direction, is justified by the large ratio of the QD diameter ≈ 70 nm to QD height < 9 nm, and is further verified by modeling two-dimensional spin diffusion (see Supplementary Section 4).

D. Effect of central spin on nuclear spin diffusion

Dividing the typical Knight shift of ≈ 50 kHz by half the QD thickness (4.5 nm) we calculate the gradient and roughly estimate the Knight shift difference of ≈ 4.4 kHz for the two nearest-neighbor spins of the same isotope separated by $a_0/\sqrt{2}$, where $a_0 = 0.565$ nm is the lattice constant. Such difference significantly exceeds the energy that can be exchanged with the dipole-dipole reservoir for a spin flip-flop to happen [25] (the dipole-dipole energy is on the order of $\approx h/T_{2,N}$, where $T_{2,N} \in [1, 5]$ ms is the nuclear spin-echo coherence time [33, 51]). Therefore, one may naively expect a Knight field gradient barrier to form and suppress spin diffusion in an electron-charged QD (since the flip-flops would be limited to the few nuclear spin pairs whose vector differences are nearly orthogonal to the Knight field gradient). By contrast, Figs. 3(c,d) show that in experiment the NSR is faster when the QD is occupied by a single electron ($1e$, solid symbols) for all studied T_{Pump} , demonstrating that no significant Knight field barrier is formed. However, in order to quantify the effect of the central spin on nuclear spin diffusion we must distinguish it from other non-diffusion NSR mechanisms introduced by the electron spin. To this end, we examine the magnetic field dependence shown in Fig. 4.

First, we examine a case where long optical pumping is used to suppress spin diffusion and highlight the non-diffusion mechanisms. Fig. 4(a) shows the experimental dependence $\Gamma_N(B_z)$ for long $T_{\text{Pump}} = 990$ s. In an empty QD ($0e$) spin diffusion is still the dominant NSR mechanisms –

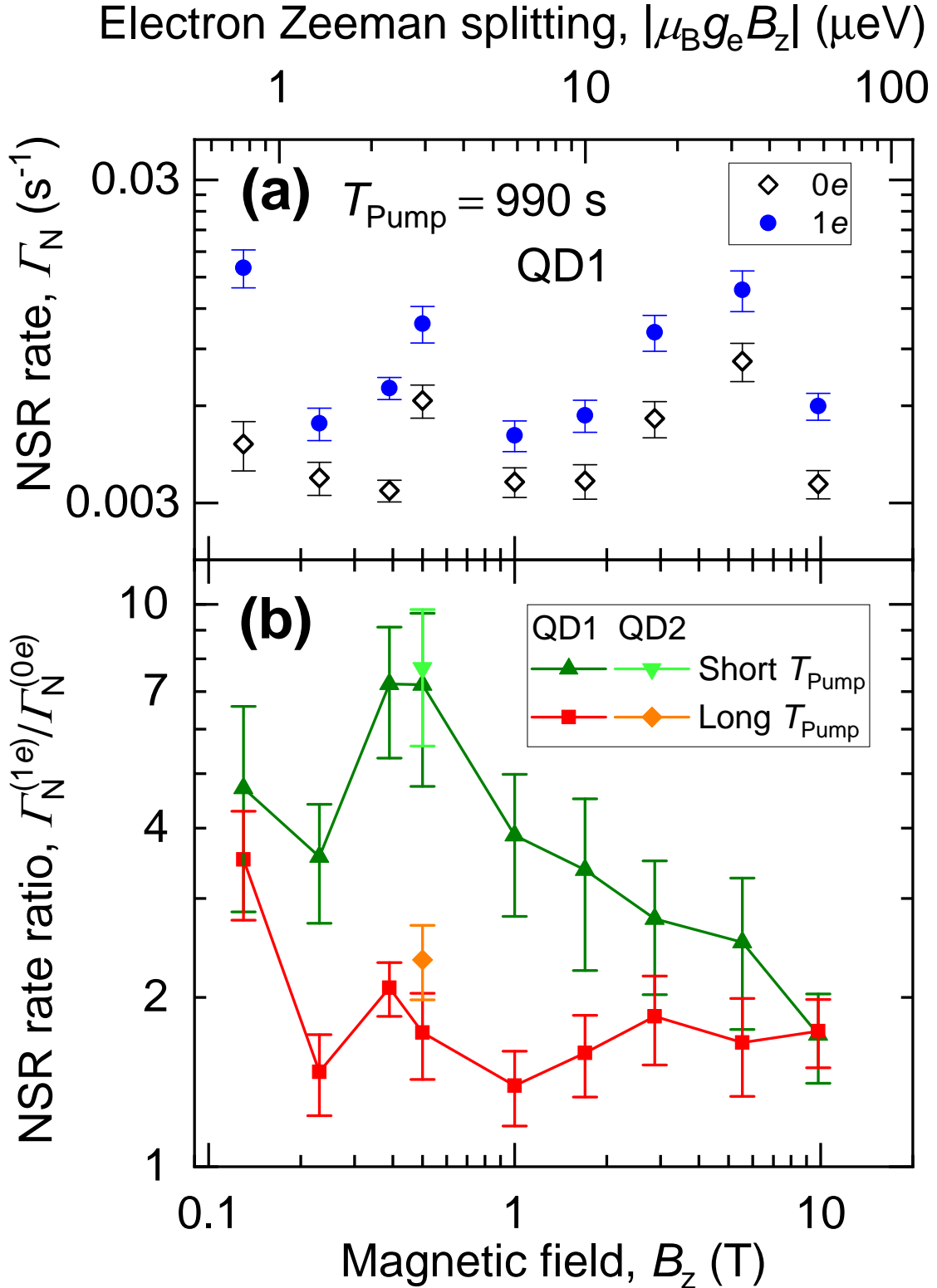


FIG. 4. (a) Nuclear spin relaxation (NSR) rate Γ_N as a function of B_Z measured in 0e (open symbols) and 1e (solid symbols) states upon long pumping $T_{\text{Pump}} = 990$ s. Top horizontal axis shows the electron Zeeman splitting at zero nuclear spin polarization. (b) Ratio $\Gamma_N^{(1e)}/\Gamma_N^{(0e)}$ of the NSR rates in 1e and 0e charge states as a function of B_Z measured under long pumping $T_{\text{Pump}} = 990$ s (squares) and short pumping $T_{\text{Pump}} \in [0.08, 0.48]$ s (triangles). All results are for the same individual dot QD1, except for the additional data from QD2 at $B_Z = 0.5$ T in (b). Error bars are 95% confidence intervals.

indeed, the observed rates $\Gamma_N^{(0e)} \in [3 \times 10^{-3}, 6 \times 10^{-3}] \text{ s}^{-1}$ are considerably higher than $\Gamma_N \in [6 \times 10^{-5}, 1 \times 10^{-3}] \text{ s}^{-1}$, found in bulk crystals [47] such as semi-insulating GaAs [16], where spin diffusion is negligible. The electron-induced rates under long pumping $\Gamma_N^{(1e)} \in [4 \times 10^{-3}, 2 \times 10^{-2}] \text{ s}^{-1}$ are nearly independent of B_z , and exceed the $0e$ rates by no more than a factor of $\Gamma_N^{(1e)}/\Gamma_N^{(0e)} < 4$ [squares in Fig. 4(b)]. Such small effect of the electron is explained by the small strain of the GaAs/AlGaAs structures, which reduces the efficiency of the non-diffusion NSR mechanisms related to phonon and electron cotunneling. This is in stark contrast to the large magnetic-field-induced variation $\Gamma_N^{(1e)} \in [5 \times 10^{-4}, 1 \times 10^1] \text{ s}^{-1}$ in Stranski-Krastanov self-assembled InGaAs QDs [50], where phonon and cotunneling mechanisms dominate, both enabled by the noncollinear hyperfine interaction [48, 50], arising in turn from the large strain-induced nuclear quadrupolar shifts. Overall, the absolute QD NSR rates shown in Fig. 4(a) are nearly constant, with some residual irregular dependence on magnetic field which we ascribe to uncontrollable parameters, such as charge state of the nearby impurities, or the initial spatial profile of the nuclear spin polarization defined by the optical nuclear spin pumping rate. By contrast, for any given B_z and T_{Pump} the ratio $\Gamma_N^{(1e)}/\Gamma_N^{(0e)}$ shown in Fig. 4(b) gives a reliable measure, which we use to examine the electron spin's effect on spin diffusion.

In order to discriminate the diffusion-related effect of the QD electron spin, in addition to the long-pumping measurements [squares in Fig. 4(b)], we choose for each magnetic field a short pumping time, typically $T_{\text{Pump}} \in [0.08, 0.48] \text{ s}$, that yields initial QD nuclear spin polarization at $\approx 1/2$ of the steady-state long-pumping polarization. The resulting short-pumping ratio $\Gamma_N^{(1e)}/\Gamma_N^{(0e)}$ is shown by the triangles in Fig. 4(b) – its excess over the long-pumping ratio $\Gamma_N^{(1e)}/\Gamma_N^{(0e)}$ is ascribed to spin diffusion alone, discriminating it from any non-diffusion mechanisms introduced by the electron spin. The electron-spin-induced acceleration of the nuclear spin diffusion is seen to be particularly pronounced at low magnetic fields $B_z \lesssim 0.5 \text{ T}$, consistent with the influence of the electron-mediated nuclear-nuclear spin interaction [23, 26, 27]. Such pairwise indirect interaction of nuclei j and k is derived from second order perturbation expansion of Eq. 1:

$$\mathcal{H}_{\text{hf},j,k}^{\text{ind}} \propto \frac{A_j A_k}{\Delta E_e} \hat{s}_z \hat{I}_j^{(+)} \hat{I}_k^{(-)}, \quad (3)$$

where $\hat{I}_j^{(\pm)} = \hat{I}_{x,j} \pm i \hat{I}_{y,j}$ and $\Delta E_e = \mu_B g_e B_z + E_{\text{hf}}$ is the electron spin splitting due to both the Zeeman effect and the nuclear-spin-induced hyperfine shift E_{hf} . In our experiments both contributions are negative, so that any nuclear spin polarization increases $|\Delta E_e|$. The rate of the indirect nuclear-nuclear spin flip-flops scales as $\propto \Delta E_e^{-2}$. Consequently, the resulting acceleration of nuclear spin diffusion in gate-defined GaAs QDs was previously found to be limited to the low

fields $B < 0.02 - 0.75$ T (Refs. [23, 27, 52]). By contrast, Fig. 4(b) shows that such acceleration persists at magnetic fields well above $B_z \gtrsim 2$ T, with short- and long-pumping $\Gamma_N^{(1e)}/\Gamma_N^{(0e)}$ ratios converging only at the maximum field $B_z = 9.82$ T.

One contributing factor is the smaller electron g -factor $g_e \approx -0.1$ (see Supplementary Section 2) and an order of magnitude smaller number of nuclei in the studied epitaxial QDs, which result in a smaller $|\Delta E_e|$ and larger A_j , respectively, when compared to the gate-defined QDs with $g_e \approx -0.4$. While these factors lead to a stronger hyperfine-mediated couplings in the studied QDs, they do not explain the magnetic field dependence: At high field $B_z = 9.82$ T the electron spin Zeeman splitting is $|\Delta E_e| \approx 58 \mu\text{eV}$, whereas at low field $B_z = 0.39$ T we take into account both the Zeeman splitting $\approx -2.3 \mu\text{eV}$ and the time-averaged hyperfine shift $E_{\text{hf}} \approx -2.5 \mu\text{eV}$ (half of the initial $E_{\text{hf}} \approx -5 \mu\text{eV}$ under the shortest used $T_{\text{Pump}} \approx 8$ ms) to estimate $|\Delta E_e| \approx 5 \mu\text{eV}$. This would correspond to a factor of $(58/5)^2 \approx 130$ reduction in the hyperfine mediated rates, while the measured short-pumping-limit NSR rate reduces only by a factor of ≈ 6 from $\Gamma_N^{(1e)} \approx 0.74 \text{ s}^{-1}$ at low field [Fig. 3(c)] to $\Gamma_N^{(1e)} \approx 0.12 \text{ s}^{-1}$ at high field [Fig. 3(d)]. Prompted by these observations, we point out that Eq. 3 treats electron spin as isolated, while in a real system the electron is coupled to external environments such as phonons and other charges. A fluctuating electron spin can accelerate nuclear spin diffusion, provided there is a frequency component in the time-dependent Knight field that equals the energy mismatch of a pair of nuclei [53, 54] – this contribution has been considered for deep impurities [14], but has been previously ignored in the context of III-V semiconductor nanostructures. For similar GaAs/AlGaAs QDs [37] the electron spin lifetime was reported to be $48 \mu\text{s}$, while for InGaAs/GaAs QDs with a similar tunnel coupling it was found to vary with magnetic field between $\approx 50 \mu\text{s}$ and a few milliseconds [50]. These lifetimes correspond to fluctuation frequencies in a [1, 10] kHz range, indeed matching the typical differences in the nuclear spin energies as revealed by NMR spectra of Fig. 2(e). Thus we speculate that the intrinsic electron spin flips, governed e.g. by the phonon relaxation and cotunneling coupling to the electron Fermi reservoir of the n -doped layer [50, 55, 56], contribute to acceleration of nuclear spin diffusion in the studied GaAs QDs, especially at high magnetic fields.

E. Comparison with previous results on nuclear spin diffusion

In order to understand what controls the rate of spin diffusion we first make a comparison with Stranski-Krastanov InGaAs/GaAs and InP/GaInP self-assembled QDs, where quadrupolar shifts are so large (MHz range [40, 57]) that all nuclear spins are essentially isolated from each other,

eliminating spin diffusion and resulting in very long nuclear spin lifetimes $T_{1,N}^{(0e)} > 10^4$ s in empty ($0e$) QDs [26, 29, 48, 50, 58, 59]. Even in presence of the electron spin ($1e$) the nuclear spin diffusion takes place only inside the QD [26, 48], without diffusion into the surrounding material.

In the lattice-matched GaAs QDs the strain-induced effects are smaller but not negligible, characterized by quadrupolar shifts ν_Q ranging approximately between 10 and 50 kHz within the QD, as revealed by NMR spectra in Fig. 2(e). Nuclei in $I_z = \pm 1/2$ and $|I_z| > 1/2$ states must be considered separately. The central transition between the $I_z = -1/2$ and $+1/2$ spin states is affected only by the second order quadrupolar shifts, which scale as $\propto \nu_Q^2/\nu_L$ and are within a few kHz for the studied range of nuclear spin Larmor frequencies $\nu_L \in [1, 130]$ MHz. These second order quadrupolar shifts are comparable to the homogeneous nuclear spin linewidth $\propto 1/T_{2,N}$, and therefore spin diffusion in GaAs/AlGaAs QDs is expected to be unimpeded for the nuclei in the $I_z = \pm 1/2$ states. By contrast, the $I_z = \pm 3/2$ spin states experience first order quadrupolar shifts ν_Q , which are tens of kHz, significantly exceeding the homogeneous NMR linewidths in the studied GaAs QDs. The resulting dynamics of the $I_z = \pm 3/2$ nuclei is therefore sensitive to nanoscale inhomogeneity of the strain-induced ν_Q . From the NSR experiments [Fig. 3(b)] we observe that nuclear spin polarization relaxes to zero, even in an empty QD ($0e$). This can only happen if spin diffusion is unimpeded not only for the $I_z = \pm 1/2$ states, but also for the $I_z = \pm 3/2$ states that are subject to the larger first order quadrupolar shifts. Our interpretation is that strain in the studied GaAs/AlGaAs QDs is a smooth function of spatial coordinates: for nearly each QD nucleus it is possible to find some neighboring nuclei with a strain variation small enough to form a chain that conducts spin diffusion out of the GaAs QD into the AlGaAs barriers.

Similarly fast NSR was observed previously in neutral QDs formed by monolayer fluctuations in GaAs/AlGaAs quantum wells [22]. However, the opposite scenario was realized in QDs with nanoholes etched in pure GaAs [43] where nuclear spin polarization in an empty QD ($0e$) was preserved for over $T_{1,N} > 5000$ s, suggesting that some of the nuclei were frozen in the $I_z = \pm 3/2$ states, akin to quadrupolar blockade of spin diffusion in self-assembled QDs. This contrast is rather remarkable since the average strain, characterized by the average $\nu_Q \approx 20 - 30$ kHz, is very similar for QDs grown in nanoholes etched in AlGaAs (studied here) and in GaAs (Ref. [43]). This comparison suggests that nuclear spin dynamics are sensitive to QD morphology down to the atomic scale, and could be affected by factors such as QD shape, as well as GaAs/AlGaAs interface roughness and intermixing [60–62]. One possible contributing factor is the QD growth temperature, which was 610° C in the structures used here, considerably higher than 520° C in the structures studied previously [42, 43]. Further work would be required to elucidate the role of all

the underlying growth parameters. Conversely, NSR can be a sensitive probe of the QD internal structure.

We now quantify the spin diffusion process and compare our results to the earlier studies in GaAs-based structures. The best fit of the experimental NSR dynamics [lines in Fig. 3(b)] yields $D_{\text{Dark}}^{(0e)} = 2.2_{-0.5}^{+0.7} \text{ nm}^2 \text{ s}^{-1}$ for the diffusion coefficient in an empty QD and in the absence of optical excitation, in agreement with $D = 1.0 \pm 0.15 \text{ nm}^2 \text{ s}^{-1}$ measured previously for spin diffusion between two GaAs quantum wells across an $\text{Al}_{0.35}\text{Ga}_{0.65}\text{As}$ barrier [34]. This is approximately an order of magnitude smaller than the first-principle estimate [63–65] of $D_{\text{Dark}}^{(0e)} \approx 19 \text{ nm}^2 \text{ s}^{-1}$ for bulk GaAs (see Supplementary Section 3) and the $D = 15.0 \pm 7 \text{ nm}^2 \text{ s}^{-1}$ value measured in pure AlAs [66]. The reduced diffusion in the AlGaAs alloy can be explained by the quadrupolar disorder, arising from the random positioning of the aluminium atoms [34]. Charging of the QD with a single electron accelerates spin diffusion: we find $D_{\text{Dark}}^{(1e)}(9.82 \text{ T}) = 4.7_{-1.0}^{+1.2} \text{ nm}^2 \text{ s}^{-1}$, which increases to $D_{\text{Dark}}^{(1e)}(0.39 \text{ T}) = 7.7 \pm 1.9 \text{ nm}^2 \text{ s}^{-1}$ at low magnetic fields where hyperfine-mediated nuclear-nuclear spin exchange is enhanced in accordance with Eq. 3. While experimental data can be well described by the spin diffusion Eq. 2, it is worth noting the limited nature of the model, which ignores the spatial variations of the nuclear-nuclear couplings, the dependence of the electrons spin splitting ΔE_e on the instantaneous nuclear spin polarization, the isotopic difference between ^{75}As , ^{69}Ga and ^{71}Ga , as well as neglecting any spin diffusion orthogonal to the sample growth z direction. As such, the diffusion coefficients D should be treated as a coarse-grained description, aggregating the numerous lattice-constant-scale parameters of the many-body spin ensemble evolution.

IV. DISCUSSION AND OUTLOOK

The GaAs/AlGaAs QDs grown by nanohole infilling combine excellent optical properties with low intrinsic strain, allowing for nuclear spin qubit and quantum memory designs [32, 33, 39]. The key performance characteristic is the nuclear spin coherence time, which can be extended up to $T_{2,N} \approx 10 \text{ ms}$ (Ref. [33]), but is ultimately limited by the longitudinal relaxation time $T_{1,N}$. Moreover, it is the state longevity of the nuclei interfaced with the QD electron spin that is relevant. Thus, one should consider the NSR time in the regime of short pumping, found here to range from $T_{1,N}^{(1e)} \approx 1 \text{ s}$ at low magnetic fields to $T_{1,N}^{(1e)} \approx 10 \text{ s}$ at high fields. For nuclear spin quantum computing with the typical $10 \mu\text{s}$ coherent control gates [33], a large number of operations $\gtrsim 10^5$ would be possible without the disruptive effect of spin diffusion.

In conclusion, we have addressed the long-standing dilemma of whether the central spin of

an electron accelerates or suppresses diffusion in a nuclear spin lattice. We have used variable-duration optical pumping [15, 17, 20, 22] to identify nuclear spin diffusion as the dominant NSR mechanism. In contrast to previous studies of nuclear spin diffusion [15, 16, 20, 21, 24, 25], we use a charge tunable structure and probe nuclear spin dynamics with and without the electron under otherwise identical conditions – importantly, our QD charge control is achieved without reverting to optical pumping [24, 25], thus eliminating the unwanted charge fluctuations. Combining these two aspects, we conclude that in a technologically important class of lattice matched GaAs/AlGaAs nanostructures the electron spin accelerates the nuclear spin diffusion, with no signature of a Knight-field-gradient barrier. We expect these findings to be relevant for a range of lattice-matched QDs [22, 23, 27, 52] and shallow impurities [16], whereas an efficient spin diffusion barrier can arise from an electron with sub-nanometer localization [14]. Future work can examine reduction of spin diffusion in low-strain nanostructures. The proximity of the n -doped layer, acting as a sink for nuclear polarization, as well as QD morphology can be optimized. Alternatively, pure AlAs barriers can be used to grow GaAs QDs with well isolated Ga nuclei, potentially offering long-lived spin memories and qubits.

ACKNOWLEDGMENTS

Acknowledgements: P.M-H. and E.A.C. were supported by EPSRC through a doctoral training grant and EP/V048333/1, respectively. E.A.C. was supported by a Royal Society University Research Fellowship. A.R. acknowledges support of the Austrian Science Fund (FWF) via the Research Group FG5, I 4320, I 4380, I 3762, the European Union’s Horizon 2020 research and innovation program under Grant Agreements No. 899814 (Qurope) and No. 871130 (Ascent+), the Linz Institute of Technology (LIT), and the LIT Secure and Correct Systems Lab, supported by the State of Upper Austria. E.A.C is grateful to René Dost for advice on sample processing. Author contributions: S.M., S.F.C.S and A.R. developed, grew and processed the quantum dot samples. P.M-H. and E.A.C. conducted the experiments. E.A.C. drafted the manuscript with input from all authors. E.A.C. coordinated the project.

-
- [1] A. S. Oja and O. V. Lounasmaa, [Rev. Mod. Phys.](#) **69**, 1 (1997).
 - [2] E. M. Kessler, G. Giedke, A. Imamoglu, S. F. Yelin, M. D. Lukin, and J. I. Cirac, [Phys. Rev. A](#) **86**, 012116 (2012).

- [3] P. G. de Gennes, P. A. Pincus, F. Hartmann-Boutron, and J. M. Winter, *Phys. Rev.* **129**, 1105 (1963).
- [4] Y. Shiomi, J. Lustikova, S. Watanabe, D. Hirobe, S. Takahashi, and E. Saitoh, *Nat. Phys.* **15**, 22 (2019).
- [5] R. Dorner, J. Goold, C. Cormick, M. Paternostro, and V. Vedral, *Phys. Rev. Lett.* **109**, 160601 (2012).
- [6] J. H. Bardarson, F. Pollmann, and J. E. Moore, *Phys. Rev. Lett.* **109**, 017202 (2012).
- [7] N. Bloembergen, *Physica* **15**, 386 (1949).
- [8] W. E. Blumberg, *Phys. Rev.* **119**, 79 (1960).
- [9] W. Zhang and D. G. Cory, *Phys. Rev. Lett.* **80**, 1324 (1998).
- [10] K. W. Eberhardt, S. Mouaziz, G. Boero, J. Brugger, and B. H. Meier, *Phys. Rev. Lett.* **99**, 227603 (2007).
- [11] W. D. Knight, *Phys. Rev.* **76**, 1259 (1949).
- [12] B. Urbaszek, X. Marie, T. Amand, O. Krebs, P. Voisin, P. Maletinsky, A. Högele, and A. Imamoglu, *Rev. Mod. Phys.* **85**, 79 (2013).
- [13] G. W. Leppelmeier and J. Jeener, *Phys. Rev.* **175**, 498 (1968).
- [14] J. P. Wolfe, *Phys. Rev. Lett.* **31**, 907 (1973).
- [15] D. Paget, *Phys. Rev. B* **25**, 4444 (1982).
- [16] J. Lu, M. J. R. Hoch, P. L. Kuhns, W. G. Moulton, Z. Gan, and A. P. Reyes, *Phys. Rev. B* **74**, 125208 (2006).
- [17] H. Hayashi, K. M. Itoh, and L. S. Vlasenko, *Phys. Rev. B* **78**, 153201 (2008).
- [18] J. J. Wittmann, M. Eckardt, W. Harneit, and B. Corzilius, *Phys. Chem. Chem. Phys.* **20**, 11418 (2018).
- [19] A. Ajoy, K. Liu, R. Nazaryan, X. Lv, P. R. Zangara, B. Safvati, G. Wang, D. Arnold, G. Li, A. Lin, P. Raghavan, E. Druga, S. Dhomkar, D. Pagliero, J. A. Reimer, D. Suter, C. A. Meriles, and A. Pines, *Science Advances* **4**, eaar5492 (2018).
- [20] R. Tycko, S. Barrett, G. Dabbagh, L. Pfeiffer, and K. West, *Science* **268**, 1460 (1995).
- [21] V. Bayot, E. Grivei, J.-M. Beuken, S. Melinte, and M. Shayegan, *Phys. Rev. Lett.* **79**, 1718 (1997).
- [22] A. E. Nikolaenko, E. A. Chekhovich, M. N. Makhonin, I. W. Drouzas, A. B. Van'kov, J. Skiba-Szymanska, M. S. Skolnick, P. Senellart, D. Martrou, A. Lemaître, and A. I. Tartakovskii, *Phys. Rev. B* **79**, 081303 (2009).
- [23] D. J. Reilly, J. M. Taylor, J. R. Petta, C. M. Marcus, M. P. Hanson, and A. C. Gossard, *Phys. Rev. Lett.* **104**, 236802 (2010).
- [24] M. N. Makhonin, E. A. Chekhovich, P. Senellart, A. Lemaître, M. S. Skolnick, and A. I. Tartakovskii, *Phys. Rev. B* **82**, 161309 (2010).
- [25] G. Sallen, S. Kunz, T. Amand, L. Bouet, T. Kuroda, T. Mano, D. Paget, O. Krebs, X. Marie, K. Sakoda, and B. Urbaszek, *Nature Communications* **5**, 3268 (2014).
- [26] D. Klauser, W. A. Coish, and D. Loss, *Phys. Rev. B* **78**, 205301 (2008).
- [27] Z.-X. Gong, Z. qi Yin, and L.-M. Duan, *New Journal of Physics* **13**, 033036 (2011).

- [28] C. Deng and X. Hu, *Phys. Rev. B* **72**, 165333 (2005).
- [29] C. W. Lai, P. Maletinsky, A. Badolato, and A. Imamoglu, *Phys. Rev. Lett.* **96**, 167403 (2006).
- [30] C. Ramanathan, *Applied Magnetic Resonance* **34**, 409 (2008).
- [31] K. Heshami, D. G. England, P. C. Humphreys, P. J. Bustard, V. M. Acosta, J. Nunn, and B. J. Sussman, *J. Mod. Opt.* **63**, 2005 (2016).
- [32] E. V. Denning, D. A. Gangloff, M. Atatüre, J. Mørk, and C. Le Gall, *Phys. Rev. Lett.* **123**, 140502 (2019).
- [33] E. A. Chekhovich, S. F. C. da Silva, and A. Rastelli, *Nat. Nanotechnol.* **15**, 999 (2020).
- [34] A. Malinowski, M. Brand, and R. Harley, *Physica E: Low-dimensional Systems and Nanostructures* **10**, 13 (2001), proceedings of the First International Conference on the Physics and Applications of Spin-Related Phenomena in Semiconductors.
- [35] P. J. Knijn, P. J. M. van Bentum, E. R. H. van Eck, C. Fang, D. L. A. G. Grimminck, R. A. de Groot, R. W. A. Havenith, M. Marsman, W. L. Meerts, G. A. de Wijs, and A. P. M. Kentgens, *Phys. Chem. Chem. Phys.* **12**, 11517 (2010).
- [36] J. Liu, R. Su, Y. Wei, B. Yao, S. F. C. d. Silva, Y. Yu, J. Iles-Smith, K. Srinivasan, A. Rastelli, J. Li, and X. Wang, *Nature Nanotech.* **14**, 586 (2019).
- [37] L. Zhai, M. C. Löbl, G. N. Nguyen, J. Ritzmann, A. Javadi, C. Spinnler, A. D. Wieck, A. Ludwig, and R. J. Warburton, *Nat. Commun.* **11**, 4745 (2020).
- [38] N. Tomm, A. Javadi, N. O. Antoniadis, D. Najer, M. C. Löbl, A. R. Korsch, R. Schott, S. R. Valentin, A. D. Wieck, A. Ludwig, and R. J. Warburton, *Nature Nanotechnology* **16**, 399 (2021).
- [39] L. Zaporski, N. Shofer, J. H. Bodey, S. Manna, G. Gillard, D. M. Jackson, M. H. Appel, C. Schimpf, S. C. da Silva, J. Jarman, G. Delamare, G. Park, U. Haeusler, E. A. Chekhovich, A. Rastelli, D. A. Gangloff, M. Atatüre, and C. Le Gall, *arXiv*, 2206.01223 (2022).
- [40] E. A. Chekhovich, K. V. Kavokin, J. Puebla, A. B. Krysa, M. Hopkinson, A. D. Andreev, A. M. Sanchez, R. Beanland, M. S. Skolnick, and A. I. Tartakovskii, *Nature Nanotech.* **7**, 646 (2012).
- [41] C. Heyn, A. Stemmann, T. Koppen, C. Strelow, T. Kipp, M. Grave, S. Mendach, and W. Hansen, *Appl. Phys. Lett.* **94**, 183113 (2009).
- [42] P. Atkinson, E. Zallo, and O. G. Schmidt, *J. Appl. Phys.* **112**, 054303 (2012).
- [43] A. Ulhaq, Q. Duan, E. Zallo, F. Ding, O. G. Schmidt, A. I. Tartakovskii, M. S. Skolnick, and E. A. Chekhovich, *Phys. Rev. B* **93**, 165306 (2016).
- [44] E. A. Chekhovich, I. M. Griffiths, M. S. Skolnick, H. Huang, S. F. Covre da Silva, X. Yuan, and A. Rastelli, *Phys. Rev. B* **97**, 235311 (2018).
- [45] I. M. Griffiths, H. Huang, A. Rastelli, M. S. Skolnick, and E. A. Chekhovich, *Phys. Rev. B* **99**, 125304 (2019).
- [46] S. E. Barrett, G. Dabbagh, L. N. Pfeiffer, K. W. West, and R. Tycko, *Phys. Rev. Lett.* **74**, 5112 (1995).
- [47] J. A. McNeil and W. G. Clark, *Phys. Rev. B* **13**, 4705 (1976).
- [48] C. Latta, A. Srivastava, and A. Imamoglu, *Phys. Rev. Lett.* **107**, 167401 (2011).

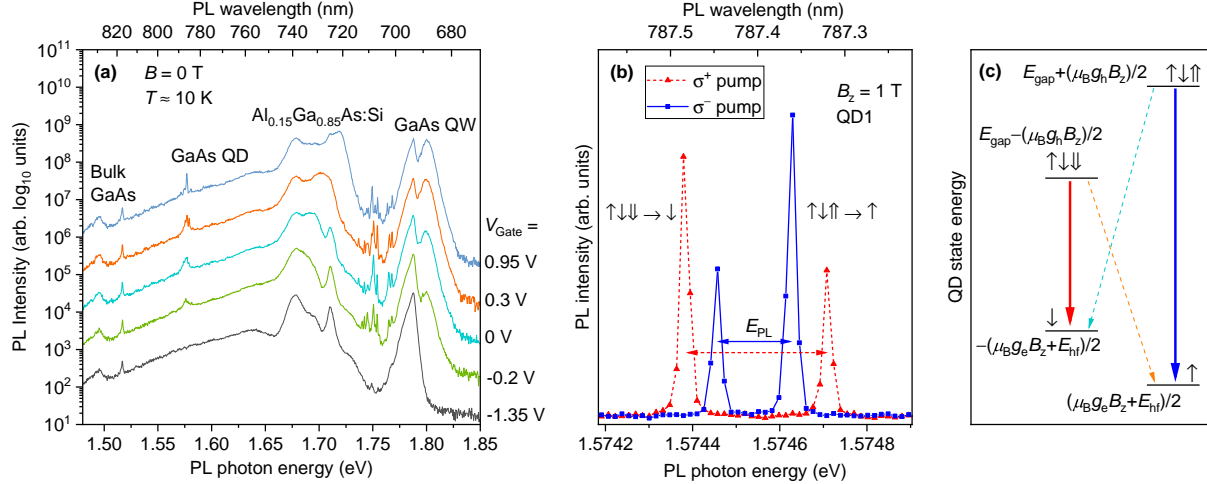
- [49] M. Vladimirova, S. Cronenberger, D. Scalbert, M. Kotur, R. I. Dzhioev, I. I. Ryzhov, G. G. Kozlov, V. S. Zapasskii, A. Lemaître, and K. V. Kavokin, [Phys. Rev. B](#) **95**, 125312 (2017).
- [50] G. Gillard, I. M. Griffiths, G. Ragnathan, A. Ulhaq, C. McEwan, E. Clarke, and E. A. Chekhovich, [npj Quantum Inf.](#) **7**, 43 (2021).
- [51] E. A. Chekhovich, M. Hopkinson, M. S. Skolnick, and A. I. Tartakovskii, [Nature Commun.](#) **6**, 6348 (2015).
- [52] F. K. Malinowski, F. Martins, L. Cywiński, M. S. Rudner, P. D. Nissen, S. Fallahi, G. C. Gardner, M. J. Manfra, C. M. Marcus, and F. Kuemmeth, [Phys. Rev. Lett.](#) **118**, 177702 (2017).
- [53] G. R. Khutsishvili, [Soviet Physics Uspekhi](#) **8**, 743 (1966).
- [54] E. P. Horvitz, [Phys. Rev. B](#) **3**, 2868 (1971).
- [55] M. Kroutvar, Y. Ducommun, D. Heiss, M. Bichler, D. Schuh, G. Abstreiter, and J. J. Finley, [Nature](#) **432**, 81 (2004).
- [56] C.-Y. Lu, Y. Zhao, A. N. Vamivakas, C. Matthiesen, S. Fält, A. Badolato, and M. Atatüre, [Phys. Rev. B](#) **81**, 035332 (2010).
- [57] C. Bulutay, [Phys. Rev. B](#) **85**, 115313 (2012).
- [58] A. Greilich, A. Shabaev, D. R. Yakovlev, A. L. Efros, I. A. Yugova, D. Reuter, A. D. Wieck, and M. Bayer, [Science](#) **317**, 1896 (2007).
- [59] E. A. Chekhovich, M. N. Makhonin, J. Skiba-Szymanska, A. B. Krysa, V. D. Kulakovskii, M. S. Skolnick, and A. I. Tartakovskii, [Phys. Rev. B](#) **81**, 245308 (2010).
- [60] B. Jusserand and F. Mollot, [Applied Physics Letters](#) **61**, 423 (1992).
- [61] A. Saher Helmy, J. S. Aitchison, and J. H. Marsh, [Applied Physics Letters](#) **71**, 2998 (1997).
- [62] W. Braun, A. Trampert, L. Däweritz, and K. H. Ploog, [Phys. Rev. B](#) **55**, 1689 (1997).
- [63] I. J. Lowe and S. Gade, [Phys. Rev.](#) **156**, 817 (1967).
- [64] A. G. Redfield and W. N. Yu, [Phys. Rev.](#) **177**, 1018 (1969).
- [65] E. R. Butkevich and R. K. Sabirov, [Physica Status Solidi \(b\)](#) **146**, 683 (1988).
- [66] M.-H. Nguyen, S. Tsuda, D. Terasawa, A. Fukuda, Y. Zheng, and A. Sawada, [Phys. Rev. B](#) **89**, 041403 (2014).

SUPPLEMENTARY MATERIAL

Supplementary Section 1. SAMPLE STRUCTURE

The sample is grown using molecular beam epitaxy (MBE) on a semi-insulating GaAs (001) substrate. The growth starts with a layer of $\text{Al}_{0.95}\text{Ga}_{0.05}\text{As}$ followed by a single pair of $\text{Al}_{0.2}\text{Ga}_{0.8}\text{As}$ and $\text{Al}_{0.95}\text{Ga}_{0.05}\text{As}$ layers acting as a Bragg reflector in optical experiments. Then, a 95 nm thick layer of $\text{Al}_{0.15}\text{Ga}_{0.85}\text{As}$ is grown. The rest of the structure follows the schematic shown in Fig. 2(c) of the main text beginning with a 95 nm thick layer of $\text{Al}_{0.15}\text{Ga}_{0.85}\text{As}$ doped with Si at a volume concentration of $1.0 \times 10^{18} \text{ cm}^{-3}$. The low Al concentration of 0.15 in the Si doped layer mitigates the issues caused by the deep DX centers [67–69]. Under optical excitation this $\text{Al}_{0.15}\text{Ga}_{0.85}\text{As}:\text{Si}$ gives rise to broad photoluminescence at around 730 nm as observed in Supplementary Fig. 5(a). The n -type doped layer is followed by the electron tunnel barrier layers: first a 15 nm thick $\text{Al}_{0.15}\text{Ga}_{0.85}\text{As}$ layer and then a 15 nm thick $\text{Al}_{0.33}\text{Ga}_{0.67}\text{As}$ layer. Aluminium droplets are grown on the surface of the $\text{Al}_{0.33}\text{Ga}_{0.67}\text{As}$ layer and are used to etch the nanoholes [70, 71]. An atomic force microscopy (AFM) image of a similar sample in Fig. 2(a) of the main text shows a typical nanohole with a depth of ≈ 6.5 nm and ≈ 70 nm in diameter. Next, a 2.1 nm thick layer of GaAs is grown to form QDs by infilling the nanoholes as well as to form the quantum well (QW) layer. Thus, the maximum height of the QDs in the growth z direction is ≈ 9 nm. Low temperature PL of QDs and QW is observed [Supplementary Fig. 5(a)] at 785 nm and 690 nm, respectively. The GaAs layer is followed by a 268 nm thick $\text{Al}_{0.33}\text{Ga}_{0.67}\text{As}$ barrier layer. Finally, the p -type contact layers doped with C are grown: a 65 nm thick layer of $\text{Al}_{0.15}\text{Ga}_{0.85}\text{As}$ with a $5 \times 10^{18} \text{ cm}^{-3}$ doping concentration, followed by a 5 nm thick layer of $\text{Al}_{0.15}\text{Ga}_{0.85}\text{As}$ with a $9 \times 10^{18} \text{ cm}^{-3}$ concentration, and a 10 nm thick layer of GaAs with a $9 \times 10^{18} \text{ cm}^{-3}$ concentration.

The sample is processed into a $p-i-n$ diode structure. Mesa structures with a height of 250 nm are formed by etching away the p -doped layers and depositing Ni(10 nm)/AuGe(150 nm)/Ni(40 nm)/Au(100 nm) on the etched areas. The sample is then annealed to enable diffusion down to the n -doped layer to form the ohmic back contact. The top gate contact is formed by depositing Ti(15 nm)/Au(100 nm) on to the p -type surface of the mesa areas. The sample gate bias V_{Gate} is the bias of the p -type top contact with respect to the grounded n -type back contact. By changing V_{Gate} the equilibrium charge state of the quantum dot is tuned using the Coulomb blockade effect. Due to the large thickness of the top $\text{Al}_{0.33}\text{Ga}_{0.67}\text{As}$ layer, the tunneling of the holes is effectively blocked, whereas tunnel coupling to the n -type layer enables deterministic charging of the quantum



Supplementary Figure 5. (a) Broad range photoluminescence (PL) spectra measured under 532 nm laser excitation at different gate biases V_{Gate} . Spectra are offset in a vertical direction (log scale) by a factor of 10 for clarity. Spectral features arising from the different parts of the sample are labeled accordingly. (b) High resolution PL spectra of a negatively charged X^- trion following σ^+ (triangles) and σ^- (squares) circularly polarized optical pumping, which creates $s_z = -1/2$ (\downarrow) and $s_z = +1/2$ (\uparrow) spin polarized electrons, respectively. The electrons transfer their spin to the nuclei via magnetic (hyperfine) interaction, resulting in a build up of negative or positive net nuclear spin polarization, respectively. Through the same hyperfine interaction, the average nuclear spin polarization shifts the $s_z = -1/2$ and $s_z = +1/2$ electron spin energy levels in the opposite directions. These (Overhauser) shifts E_{hf} lead to the observed change in the spectral splitting of the trion PL, where the two components of the doublet correspond to an electron-hole recombination in presence of another electron in a $s_z = -1/2$ or $s_z = +1/2$ state. (c) Energy level diagram. The electron ground state is split by the Zeeman energy $\mu_B g_e B_z$ and the hyperfine shift E_{hf} . The X^- trion energy includes the QD bandgap energy E_{gap} and the Zeeman splitting of the unpaired hole with a positive (\uparrow) or negative (\downarrow) momentum projection. The valence band hole hyperfine effect can be neglected due to its smaller magnitude [72]. The electron and hole g -factors are g_e and g_h , respectively, with $|g_h| \gg |g_e|$ in the studied QDs. Solid arrows depict the two optically allowed transitions responsible for the spectral doublet in (b). The dashed lines show the two forbidden “diagonal” transitions.

dots with electrons.

Supplementary Section 2. EXPERIMENTAL DETAILS AND ADDITIONAL RESULTS

The sample is placed in a liquid helium bath cryostat. A superconducting coil is used to apply magnetic field up to $B_z = 10$ T. The field is parallel to the sample growth direction and the optical axis z (Faraday geometry). We use confocal microscopy configuration. An aspheric lens with a

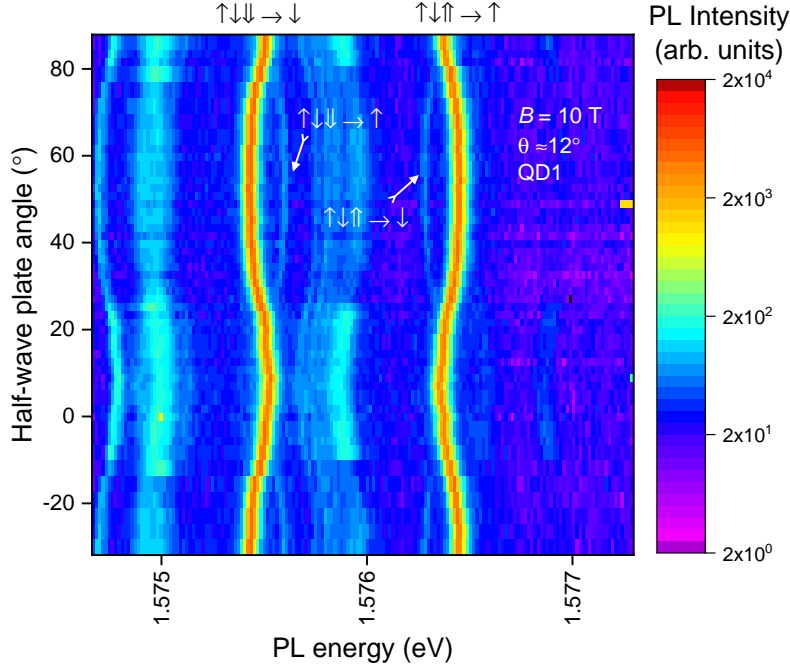
focal distance of 1.45 mm and NA=0.58 is used as an objective for optical excitation of the QD and for photoluminescence (PL) collection. The excitation laser is focused into a spot with a diameter of $\approx 1 \mu\text{m}$. The collected PL is dispersed in a two-stage grating spectrometer, each stage with a 0.85 m focal length, and recorded with a charge-coupled device (CCD) camera. The changes in the spectral splitting of a negatively charged trion X^- , derived from the PL spectra, are used to measure the hyperfine shifts E_{hf} proportional to the nuclear spin polarization degree.

Investigation of spin diffusion relies on the ability to prepare a reproducible spatial distribution of the nuclear spin polarization. This is achieved with a radiofrequency (RF) erase pulse (Fig. 3(a) of the main text) which effectively resets the nuclear spin polarization to zero in the entire sample by saturating the nuclear magnetic resonance of the As and Ga isotopes. The required oscillating magnetic field $B_x \perp z$ is produced by a coil placed at a distance of ≈ 0.5 mm from the QD sample. The coil is made of 10 turns of a 0.1 mm diameter enameled copper wire wound on a ≈ 0.4 mm diameter spool in 5 layers, with 2 turns in each layer. The coil is driven by a class-A RF amplifier (rated up to 20 W) which is fed by the output of an arbitrary waveform generator. The spectrum of the RF excitation consists of three bands, each 340 kHz wide and centered on the NMR frequency of the corresponding As or Ga isotope. Each band is generated as a frequency comb [72] with a mode spacing of 120 Hz, much smaller than the homogeneous NMR linewidth. The RF power density in the comb is chosen to be low enough and the RF pulse duration long enough (ranging between 0.1 and 10 s depending on magnetic field) to achieve noncoherent exponential depolarization of the nuclear spin ensemble.

Optical pumping of the QD nuclear spin polarization is achieved using the emission of a 690 nm circularly polarized diode lasers, which is resonant with the GaAs QW states, as seen in Supplementary Fig. 5(a). It is therefore possible that optical pumping results in dynamical nuclear polarization not only in the QDs but also in the adjacent parts of the QW. On the other hand, the pump laser photon energy is well below the bandgap of the AlGaAs barriers. For that reason we assume that dynamic nuclear polarization in AlGaAs is induced only through spin diffusion from the GaAs layer of the QW and QDs. During the pump the sample gate is set to a large reverse bias, typically $V_{\text{Gate}} = -2$ V. The pump power is $\approx 300 \mu\text{W}$, which is two orders of magnitude higher than the ground-state PL saturation power. The resulting hyperfine shifts do not exceed $|E_{\text{hf}}| < 50 \mu\text{eV}$, corresponding to initial nuclear spin polarization degree within $|P_{\text{N},0}| \lesssim 0.4$. While polarization as high as $P_{\text{N},0} \approx 0.8$ is possible [73], we deliberately use lower values to ensure linear regime of spin diffusion, free from hyperpolarization regime corrections [74]. For optical probing of the nuclear spin polarization we use a diode laser emitting at 640 nm. Sample forward bias, typi-

cally +0.5 V, and the probe power are chosen to maximize (saturate) PL intensity of the ground state X^- trion. The duration of the probe pulse, typically 20 ms, is selected to ensure minimal (few percent) depolarization of the nuclear spins during probing. Supplementary Fig. 5(b) shows X^- PL probe spectra measured at $B_z = 1$ T following optical pumping with σ^+ (triangles) and σ^- (squares) circular polarization. The difference in spectral splitting of the X^- trion doublet reveals the hyperfine shifts E_{hf} [see energy level diagram in Supplementary Fig. 5(c)]. These shifts are used to monitor the average QD nuclear spin polarization in NSR experiments such as shown in Fig. 3(b) of the main text.

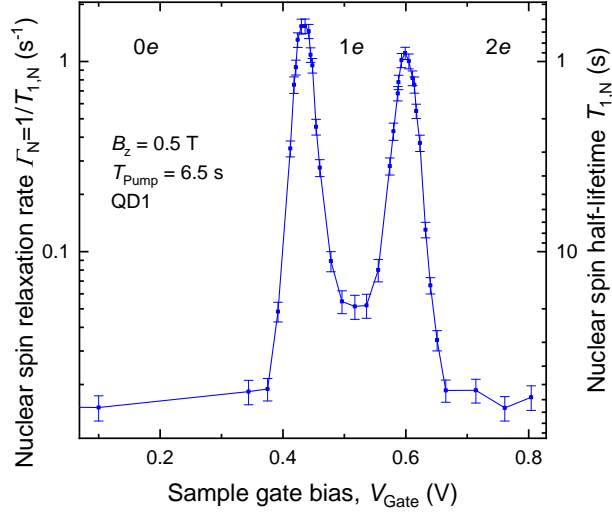
The energy splitting of the two electron spin states ΔE_e is a sum of the Zeeman splitting $\mu_B g_e B_z$ (where μ_B is the Bohr magneton) and the hyperfine splitting E_{hf} , arising from the nuclear spin polarization. We quantify the g -factor g_e of a resident electron using photoluminescence spectroscopy of a negatively charged trion. In Faraday geometry, two out of four optical transitions are forbidden, so that only the difference $g_h - g_e$ of the heavy hole and electron g -factors can be accessed. In order to derive the individual g -factors, we measure photoluminescence in oblique field configuration, where the sample growth axis is tilted by $\theta \approx 12^\circ$ away from the static magnetic field. In this configuration the “diagonal” transitions, shown by the dashed lines in Supplementary Fig. 5(c), become weakly allowed. Owing to the nearly vanishing electron g -factor in this type of GaAs/AlGaAs QDs [75], all four X^- transitions can be resolved in our setup only in high magnetic field $B = 10$ T and in presence of the optically induced hyperfine shifts. The experiment is conducted using an optical pump-probe method. The probe PL spectra are shown in Supplementary Fig. 6 as a function of the half-wave plate angle. The angle is varied to control the degree of circular polarization of the pump laser and the resulting hyperfine shift E_{hf} . The two weak transitions (labeled by the arrows) become visible when the splitting of the two bright transitions is maximized by the hyperfine shift. We further measure the spectral splitting of the two bright transitions after RF depolarization of the nuclei, which results in $E_{\text{hf}} \approx 0$. It is then possible to perform linear fit of the PL energies of all four X^- transitions and derive the g -factors. For QD1 studied in the main text and examined in Supplementary Fig. 6 we find the 95% confidence estimate $g_e \approx -0.101 \pm 0.007$ for the g -factor of a single resident electron. From the hole spin splitting of X^- at $B = 10$ T we estimate the hole g -factor in presence of two electrons as $g_h \approx +1.68$. This value should be treated as a rough estimate because of the significant nonlinearity in hole Zeeman splitting for this type of QDs [75]. We also measure the g -factors in a neutral exciton X^0 , using PL of the dark states: we find $g_e \approx -0.090 \pm 0.035$ for the electron in presence of one hole. It is notable that the electron g -factor is nearly unaffected by the extra hole [76]. Using PL spectroscopy of



Supplementary Figure 6. Photoluminescence spectra of a negatively charged trion X^- measured in oblique magnetic field $B = 10$ T tilted by $\theta \approx 12^\circ$ from the Faraday geometry. The measurement uses a pump-probe protocol, where the angle of a half-wave plate on the pump laser is varied, while the probe laser is used to detect the resulting changes in PL spectrum. The two bright lines correspond to the two allowed transitions. When the circularly polarized pump generates a sufficiently large hyperfine shift, the two weakly allowed trion transitions, labeled by the arrows, become resolved. Fitting of the PL energies reveals the electron and hole g -factors. Other (broad) spectral features correspond to PL of excitons charged with more than one electron.

the X^- trion state, we have measured g -factors in two more QDs from the same sample to find $g_e \approx -0.077 \pm 0.018$ and $g_e \approx -0.107 \pm 0.002$ for a resident electron in QD2 and QD3, respectively. From the X^0 PL of QD2 we find $g_e \approx -0.12 \pm 0.01$ for an electron in presence of a hole, whereas no dark excitons could be observed in QD3. The g -factors found here are in good agreement with the previous studies on the samples where QDs were grown in nanoholes etched in pure GaAs [75].

The sample gate bias V_{Gate} is controlled by the output of an arbitrary waveform generator connected through a 1.9 MHz low pass filter. During the dark evolution time T_{Dark} the bias can be set to an arbitrary value. For an empty dot regime ($0e$) we use large reverse bias $V_{\text{Gate}} = -1.3$ V. The bias corresponding to $1e$ Coulomb blockade is found by measuring the bias dependence of $I_{\text{N}}(V_{\text{Gate}})$ such as shown in Supplementary Fig. 7. In agreement with the previous studies on InGaAs QDs [77, 78] we observe tunnelling peaks (at ≈ 0.43 V and ≈ 0.6 V), where the electron

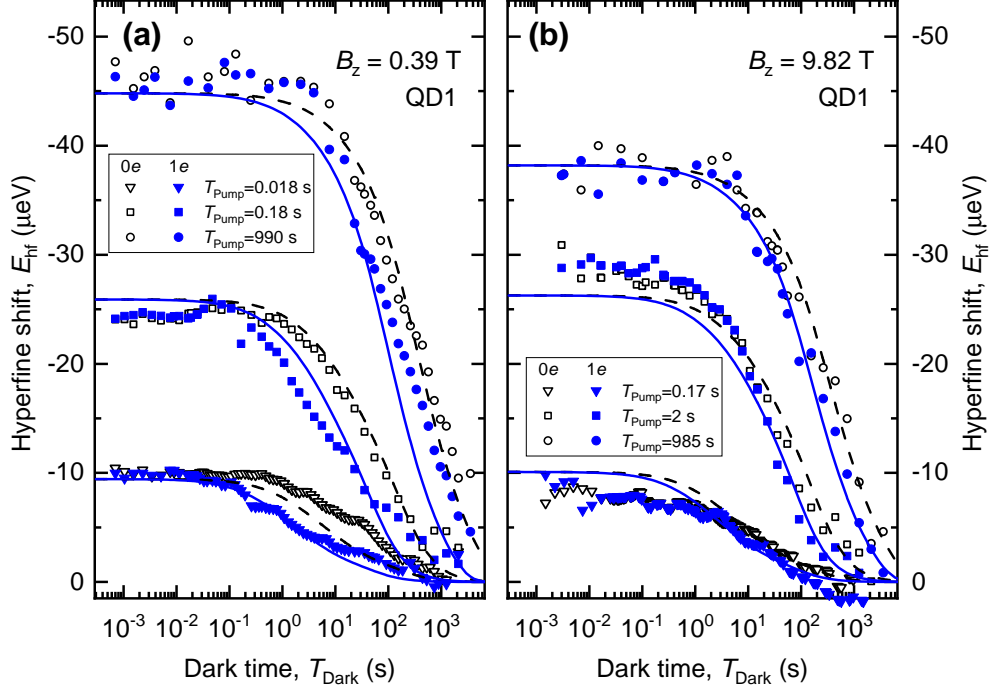


Supplementary Figure 7. Bias dependence of the nuclear spin relaxation rate Γ_N .

Fermi reservoir energy matches the QD charging energy. A bias at the middle of the Coulomb valley between the peaks, 0.517 V in this case, is used to charge the QD with one electron ($1e$). Supplementary Fig. 7 shows that when the QD is charged with two electrons ($2e$) the NSR rate is identical to the $0e$ case, confirming that the NSR acceleration produced by the single electron ($1e$) is related to its spin.

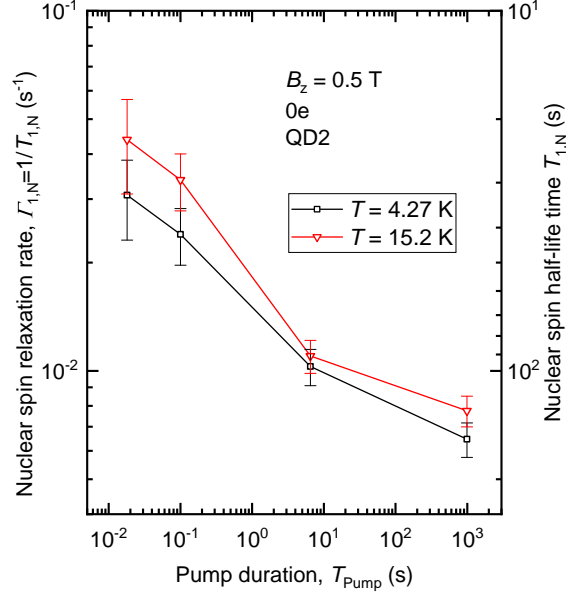
Optical pump and probe pulses are formed by mechanical shutters with a switching time of a few milliseconds. Under certain regimes in B_z and V_{Gate} this is comparable to the nuclear spin relaxation times $T_{1,N}$. However, the relaxation time in an empty QD ($0e$) is always considerably longer. Thus we keep QD under $0e$ bias during the shutter switching times and the dark time T_{Dark} is implemented by pulsing the gate bias to the target dark-state value V_{Gate} for a duration T_{Dark} .

Nuclear magnetic resonance (NMR) characterization (Fig. 2(e) of the main text) is conducted using inverse NMR method [79] which enhances the signal for $I > 1/2$ spins and improves the signal to noise ratio. In this method the nuclei are depolarized by a weak RF field, whose spectral profile is a broadband frequency comb with a narrow gap of width w_{gap} . The value of w_{gap} controls the balance between NMR amplitude and spectral resolution. In an empty QD ($0e$), NMR spectra of As and Ga measured with $w_{\text{gap}} = 6$ kHz consist of well-resolved quadrupolar-split triplets, consistent with previous observations for similar QD structures [75, 80]. The spin of a single electron ($1e$) leads to inhomogeneous Knight shifts comparable to the quadrupolar splitting. As a result, the NMR triplets are no longer resolved (solid circles in Fig. 2(e) of the main text). Moreover, the electron spin lifetime, which is on the order of milliseconds in the studied QDs, is much shorter



Supplementary Figure 8. (a) Dark time dependence of the hyperfine shift E_{hf} , which probes average nuclear spin polarization weighted by the QD electron density $|\psi_e|^2$. Nuclear spin decay is measured (symbols) at $B_z = 0.39$ T for different pumping times T_{Pump} while keeping QD empty ($0e$, open symbols) or electron-charged ($1e$, solid symbols) during the dark time. Lines show numerical solution of the spin diffusion equation. (b) Same as (a) but for $B_z = 9.82$ T.

than the radio frequency burst (typically 0.18 s), and the average electron spin polarization is therefore close to 0. Each nucleus then experiences both positive and negative Knight shifts during the RF burst. These dynamic spectral shifts disrupt the enhancement of the inverse NMR method: for example, if a nuclear spin transition fits into the RF spectral gap w_{gap} under one sign of the Knight shift, it may be moved out of the gap and into resonance with the depolarizing RF field under the opposite Knight shift. As a result, the NMR spectrum amplitude is reduced in the $1e$ measurement. By varying the gap width w_{gap} , we find that a spectrum with a reasonable signal to noise ratio is obtained at $w_{\text{gap}} = 70$ kHz, as shown by the circles in Fig. 2(e) of the main text. Although the deterioration of the inverse NMR method precludes an accurate measurement of the NMR lineshape in presence of the electron, the overall width ≈ 50 kHz of the resonance still provides a valid order-of-magnitude estimate of the Knight shifts experienced by the nuclear spins in the QD. More sophisticated measurements, using pulsed NMR (to be reported separately elsewhere) confirm this rough estimate based on inverse NMR measurement.



Supplementary Figure 9. Fitted QD nuclear spin half-life times $T_{1,N}$ (right scale) and corresponding NSR rates $\Gamma_N = 1/T_{1,N}$ (left scale) measured for different pumping times T_{Pump} at $B_z = 0.5$ T. Experiments are conducted at base sample temperature ($T = 4.27$ K, squares) and an elevated temperature ($T = 15.2$ K, triangles).

The QD NSR curves measured at $B_z = 0.39$ T and shown in Fig. 3(b) of the main text are reproduced in Supplementary Fig. 8(a), together with the similar measurements carried out at high magnetic field $B_z = 9.82$ T and shown in Supplementary Fig. 8(b). Similar to the low fields, at $B_z = 9.82$ T shorter optical pumping time T_{Pump} results in faster NSR through spin diffusion. However, the acceleration of NSR in presence of a single electron ($1e$) is less pronounced at high magnetic field, owing to the reduction of the hyperfine-mediated nuclear-nuclear spin interaction. It is also worth noting that the optical spin pumping becomes slower at high magnetic field. While $T_{\text{Pump}} = 0.018$ s at $B_z = 0.39$ T is sufficient to achieve $\approx 1/4$ of the steady state nuclear spin polarization, it takes an order of magnitude longer $T_{\text{Pump}} = 0.17$ s to reach the same $\approx 1/4$ level at $B_z = 9.82$ T. This difference limits the shortest T_{Pump} for which NSR dynamics can be measured at high magnetic field, as can be seen in Fig. 3(d) of the main text.

The experiments presented in the main text are conducted at the cryostat base temperature, measured with a resistive sensor to be $T \approx 4.27$ K. Additional measurements, similar to those shown in Fig. 3(c,d) of the main text, have been conducted on an empty QD ($0e$) at an elevated temperature $T = 15.2$ K and are shown in Supplementary Fig. 9. We find that at high temperature the relaxation rate follows the same trend of reduction at short pumping times T_{Pump} ,

consistent with NSR dominated by spin diffusion. In case of a pure spin diffusion driven by nuclear dipole-dipole interactions, one would expect the rate to be independent of the temperature. From Supplementary Fig. 9 we find that for any given T_{Pump} the relaxation is slightly accelerated at $T = 15.2$ K. One possibility is the temperature dependence of the optical nuclear spin pumping process [81] creating different spatial distributions of the nuclear spin polarization for the same T_{Pump} . Contribution of the temperature-dependent non-diffusion mechanisms, such as two-phonon quadrupolar relaxation [82, 83], is also possible.

Supplementary Section 3. FIRST PRINCIPLE ESTIMATE OF THE GaAs NUCLEAR SPIN DIFFUSION COEFFICIENT

In the absence of free electrons, nuclear spin diffusion is driven by the dipole-dipole magnetic nuclear spin interaction. The total dipole-dipole Hamiltonian term is a sum of pairwise couplings:

$$\mathcal{H}_{\text{DD}} = \sum_{i < j} b_{i,j} \left(2\hat{I}_{z,i}\hat{I}_{z,j} - \hat{I}_{x,i}\hat{I}_{x,j} - \hat{I}_{y,i}\hat{I}_{y,j} \right),$$

$$b_{i,j} = \frac{\mu_0}{4\pi} \frac{\gamma_i \gamma_j}{2} \frac{1 - 3 \cos^2 \theta_{i,j}}{r_{i,j}^3}, \quad (\text{S4})$$

where $\mu_0 = 4\pi \times 10^{-7} \text{ NA}^{-2}$ is the magnetic constant and $r_{i,j}$ denotes the length of the vector, which forms an angle θ with the static magnetic field direction (z) and connects the two spins i and j . The typical magnitude of the interaction constants for the nearby nuclei in GaAs is $\max(|b_{j,k}|)/h \approx 100$ Hz. The Hamiltonian of Eq. S4 has been truncated to eliminate all spin non-conserving terms, which is justified for static magnetic fields exceeding $\gtrsim 1$ mT, as used in this work. The evolution of a large nuclear spin ensemble can be described in terms of spin diffusion with coefficient D . In crystalline solids the nuclear spin diffusion coefficient D , is a rank-2 tensor which can be calculated from the first principles using density matrix approach [84] or the method of moments [85, 86]. The calculation involves a somewhat lengthy evaluation of the various lattice sums. Here we use a more recent version of the method of moments from Ref. [87]. We re-evaluate numerically the sums of Eqns. 8 and 10 from Ref. [87] using an FCC lattice of 6859 spins. Our results are in good agreement with the those derived for 1330 neighboring spins previously [87]. We find the following values for the diagonal components of D : $D_{xx} = D_{yy} \approx 0.2594 \frac{\mu_0}{4\pi} \frac{\hbar \gamma^2}{a_0} \rho^{1/3}$ and $D_{zz} \approx 0.3289 \frac{\mu_0}{4\pi} \frac{\hbar \gamma^2}{a_0} \rho^{1/3}$, where \hbar is the reduced Planck's constant, $a_0 \approx 0.565$ nm is the GaAs lattice constant, and γ is the nuclear gyromagnetic ratio. Here we use the coordinate system aligned with the cubic crystal axes $x \parallel [100]$, $y \parallel [010]$, $z \parallel [001]$, and the strong magnetic field is

parallel to the z direction. We have also introduced the correction factor $\rho^{1/3}$ to account for the increase of the average internuclear distance for the isotope whose abundance ρ is less than unity.

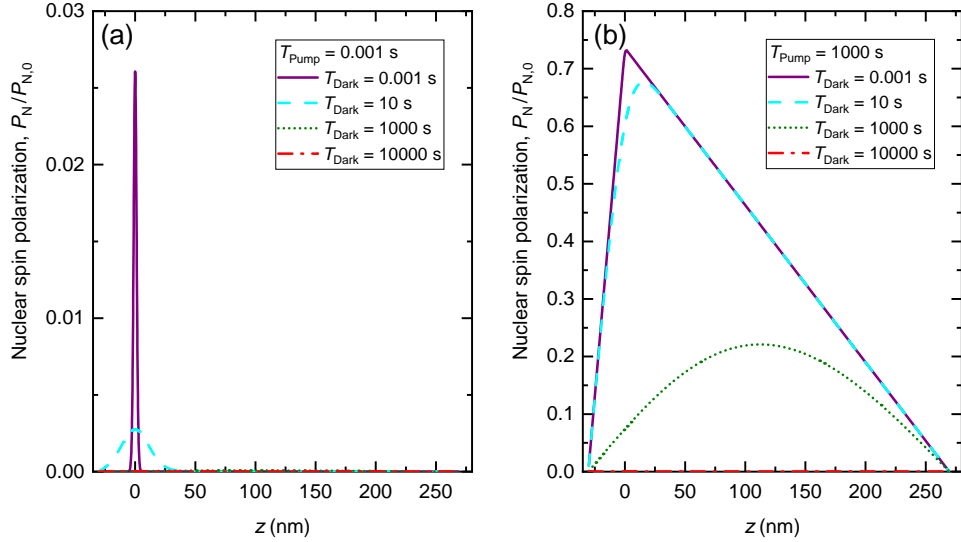
In case of arsenic, ^{75}As is the only stable isotope, so that $\rho = 1$. For gallium isotopes we have the natural abundances $\rho = 0.601$ and $\rho = 0.399$ for ^{69}Ga and ^{71}Ga , respectively. The gyromagnetic ratios γ are known [88] and, since we approximate the spin diffusion as a one-dimensional process along the sample growth direction z , we are interested in the D_{zz} component of the tensor. Substituting the numerical values we find $D_{zz} \approx 13, 21, 30 \text{ nm}^2 \text{ s}^{-1}$ for ^{75}As , ^{69}Ga and ^{71}Ga , respectively. The experiments presented in this work do not resolve between spin diffusion of the individual isotopes. As a simple approximation we can treat the observed NSR dynamics as a result of spin diffusion within one type of nuclei but with a weighted average diffusion constant. We use as weights the relative contributions of the isotopes to the optically measured hyperfine shift E_{hf} . From the previous studies of the similar QDs [73] these contributions are estimated as 0.49, 0.28 and 0.23 for ^{75}As , ^{69}Ga and ^{71}Ga , respectively, from where the average diffusion coefficient is approximated as $D_{zz} \approx 19 \text{ nm}^2$.

Supplementary Section 4. NUMERICAL SIMULATION OF NUCLEAR SPIN DIFFUSION COEFFICIENT AND ADDITIONAL ANALYSIS

The spatiotemporal evolution of the nuclear spin polarization degree $P_{\text{N}}(t, z)$ is modeled by solving the partial differential spin diffusion equation

$$\frac{\partial P_{\text{N}}(t, z)}{\partial t} = D(t) \frac{\partial^2 P_{\text{N}}(t, z)}{\partial z^2} + w(t) |\psi_{\text{e}}(z)|^2 (P_{\text{N},0} - P_{\text{N}}(t, z)), \quad (\text{S5})$$

where the last term describes optical nuclear spin pumping with a rate proportional to electron density $|\psi_{\text{e}}(z)|^2$ and the time-dependent factor $w(t)$ equal to 0 or w_0 when optical pumping is off or on, respectively. The spin diffusion coefficient $D(t)$ also takes two discrete values D_{Dark} or D_{Pump} when optical pumping is off or on, respectively. $P_{\text{N},0}$ is a steady state nuclear spin polarization degree that optical pumping would generate in the absence of spin diffusion. At each time point we assume the same diffusion coefficient D across the entire structure. The equation describes a one-dimensional problem where diffusion can take place only along the z coordinate so that the nuclear spin polarization degree P_{N} does not depend on x or y . The GaAs QD layer is modeled by taking a Gaussian profile for the electron density $|\psi_{\text{e}}(z)|^2 \propto 2^{-\left(\frac{z-z_0}{h_{\text{QD}}/2}\right)^2}$, where h_{QD} is the full width at half maximum of the $|\psi_{\text{e}}(z)|^2$ function and the center of the QD is set to be $z_0 = 0$. We use Dirichlet boundary condition $P_{\text{N}} = 0$ to model fast nuclear spin depolarization in presence of the free carriers



Supplementary Figure 10. Calculated normalized nuclear spin polarization as a function of the z coordinate at different T_{Dark} . (a) Calculations for $T_{\text{Pump}} = 1$ ms. (b) Same calculations for $T_{\text{Pump}} = 1000$ s.

both in the n - and p -type doped layers. The boundary coordinates where Dirichlet conditions are enforced are chosen to match the actual sample structure as described in [Supplementary Section 1](#). We note that the hyperfine interaction of the valence band holes is approximately 10 times weaker than for the conduction band electrons [72]. Moreover, the p -type layer is approximately 10 times further away from the QDs than the n -type layer. As a result the dynamics of the nuclear spin polarization at the QD are dominated by the n -type layer, while the exact boundary condition at the p -type layer is less crucial, justifying the use of the Dirichlet condition at both doped layers.

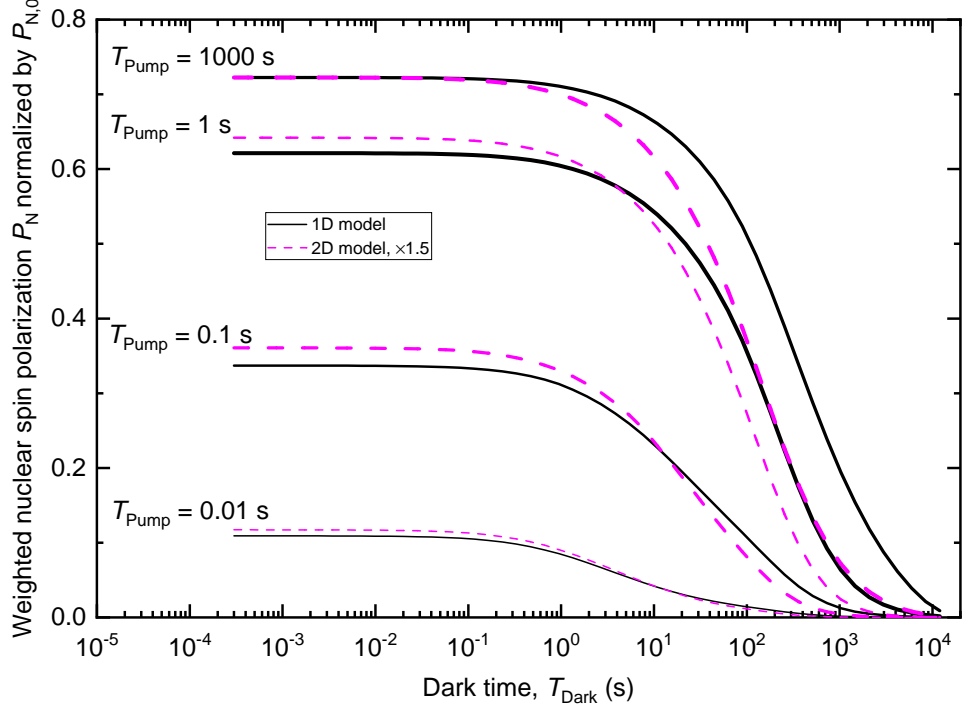
Supplementary Eq. S5 is solved numerically using the method of lines implemented in WOLFRAM MATHEMATICA 12.0. The initial condition is taken to be $P_N = 0 \forall z$, which models the result of the RF Erase pulse at the start of each measurement cycle. Optical nuclear spin pumping starts at $t = -T_{\text{Pump}}$ and the equation is solved until $t = 0$ with $D = D_{\text{Pump}}$ and $w = w_0$. At $t = 0$ optical pumping is switched off by setting $w = 0$ and the equation is solved until $t = T_{\text{Dark}}$ with $D = D_{\text{Dark}}$. Supplementary Fig. 10 shows the calculated spatial profiles of the final nuclear spin polarization $P_N(T_{\text{Dark}}, z)$ normalized by its steady-state value $P_{N,0}$. The results are shown for several T_{Dark} values in case of a short pumping [(a), $T_{\text{Pump}} = 1$ ms] and long pumping [(b), $T_{\text{Pump}} = 1000$ s]. Short pumping results in a small-magnitude ($P_N \ll P_{N,0}$) spatially-narrow nuclear spin polarization, which quickly dissipates at $t > 0$. By contrast, long pumping leads to a steady-state spatial distribution where polarization peaks at the quantum dot coordinate $z = 0$ and reduces linearly towards the doped layers which act as nuclear spin polarization sinks.

Interestingly, this calculation predicts that the maximum polarization $P_{N,0}$ is not achieved because of the diffusion towards the doped layers, especially the closely located n -type layer at $z < 0$.

In order to compare simulations with the experimental results the final spatial distribution $P_N(T_{\text{Dark}}, z)$ is multiplied by $|\psi_e(z)|^2$ and integrated over z . This way we reproduce the optical probing of the nuclear spin polarization, where the measured hyperfine shift E_{hf} is effectively weighted by the electron envelope wavefunction density $|\psi_e(z)|^2$. The simulated hyperfine shift is then derived as $E_{\text{hf}} = E_{zX^-} + AIP_N$, where I is the nuclear spin number, A is the hyperfine constant and E_{zX^-} is the trion Zeeman splitting in the absence of nuclear spin polarization. We then use a differential evolution algorithm to vary the parameters such as $D_{\text{Dark}}^{(ne)}(B_z)$, $w_0(B_z)$ and $D_{\text{Pump}}(B_z)$ and fit the simulated E_{hf} dynamics to the entire experimental datasets of $E_{\text{hf}}(T_{\text{Pump}}, T_{\text{Dark}})$ measured at $B_z = 0.39$ and 9.82 T for empty ($n = 0$) and charged ($n = 1$) QD states. As discussed in the main text the best-fit diffusion coefficients in the dark are $D_{\text{Dark}}^{(0e)} = 2.2_{-0.5}^{+0.7} \text{ nm}^2 \text{ s}^{-1}$ independent of magnetic field, $D_{\text{Dark}}^{(1e)}(9.82 \text{ T}) = 4.7_{-1.0}^{+1.2} \text{ nm}^2 \text{ s}^{-1}$ and $D_{\text{Dark}}^{(1e)}(0.39 \text{ T}) = 7.7 \pm 1.9 \text{ nm}^2 \text{ s}^{-1}$. For spin diffusion coefficients under optical pumping we find significantly larger values $D_{\text{Pump}}^{(1e)}(9.82 \text{ T}) = 96_{-28}^{+44} \text{ nm}^2 \text{ s}^{-1}$ and $D_{\text{Pump}}^{(1e)}(0.39 \text{ T}) = 850_{-220}^{+240} \text{ nm}^2 \text{ s}^{-1}$. This can be ascribed to the spectrally broad fluctuations of the optically generated electron spins which provide coupling between the distant nuclear spins, thus facilitating the diffusion. The other best-fit parameters are $w_0(0.39 \text{ T}) = 37_{-5}^{+7} \text{ s}^{-1}$, $w_0(9.82 \text{ T}) = 5.7_{-0.9}^{+1.1} \text{ s}^{-1}$ and $h_{\text{QD}} = 2.1_{-0.2}^{+0.3} \text{ nm}$. Previous studies on GaAs/AlGaAs QDs emitting at a similar wavelength estimated that 0.92 of the electron density resides in the GaAs layer [73], whose full width can then be estimated as $h_{\text{QD}} \frac{\text{erf}^{-1}(0.92)}{\sqrt{\ln(2)}} = 3.2_{-0.3}^{+0.4} \text{ nm}$. This best-fit value somewhat underestimates the true QD thickness in z direction, but is within the range bounded by the QW thickness (2.1 nm) and the maximum QD thickness ($\approx 9 \text{ nm}$) estimated from the nanohole depth in AFM. The spatial profiles shown in Supplementary Fig. 10 are calculated with the best-fit parameters for the $1e$ case at $B_z = 0.39 \text{ T}$.

The use of the one dimensional spin diffusion model is motivated by the large aspect ratio of the QD: the diffusion proceeds predominantly along the direction of the strongest gradient in the nuclear spin polarization degree, which is the growth z direction. For numerical simulations, one dimensional model is also advantageous as it requires significantly less computational resources than a full three dimensional diffusion model. In order to evaluate the limitations of the one dimensional model we run a simulation of a two dimensional diffusion problem, where the equation now reads:

$$\frac{\partial P_N(t, x, z)}{\partial t} = D(t) \left(\frac{\partial^2 P_N(t, x, z)}{\partial x^2} + \frac{\partial^2 P_N(t, x, z)}{\partial z^2} \right) + w(t) |\psi_e(x, z)|^2 (P_{N,0} - P_N(t, x, z)) \quad (\text{S6})$$



Supplementary Figure 11. Numerically simulated nuclear spin polarization degree P_N weighted by the electron envelope wavefunction density $|\psi_e(z)|^2$ and normalized by the maximum nuclear spin polarization $P_{N,0}$ in the absence of spin diffusion. The weighted polarization is plotted as a function of the dark time T_{Dark} for different T_{Pump} . The results are shown for the case of one dimensional diffusion (1D, solid lines) and two dimensional diffusion (2D, dashed lines, P_N values multiplied by 1.5).

The electron density is taken to be $|\psi_e(x, z)|^2 \propto 2^{-\left(\frac{x-x_0}{d_{\text{QD}}/2} + \frac{z-z_0}{h_{\text{QD}}/2}\right)^2}$, where d_{QD} is a full width at half maximum diameter of the QD, which we set to $d_{\text{QD}} = 47$ nm in order to match the 0.92 electron wavefunction density in a QD with a full diameter of 70 nm. The same $|\psi_e(x, z)|^2$ is used to calculate the weighted nuclear spin polarization degree, emulating the optical probing of the QD hyperfine shift E_{hf} . The computational domain is limited to $|x| < 700$ nm and we implement the additional Dirichlet boundary condition $P_N(x = \pm 700 \text{ nm}) = 0$.

Supplementary Fig. 11 shows the simulated QD NSR dynamics in a one dimensional (1D, solid lines) and two dimensional (2D, dashed lines) cases, following nuclear spin pumping with different durations T_{Pump} . One difference in the resulting dynamics is the lower weighted nuclear spin polarization degree within the QD volume in the 2D case. Consequently, all the 2D-case P_N values in Supplementary Fig. 11 have been multiplied by 1.5, to simplify comparison with the 1D case. At short $T_{\text{Pump}} \leq 0.1$ s QD nuclear spin polarization decays on the same timescale both in 1D and 2D cases. This is expected: the spatial profile of the nuclear spin polarization produced by

short pumping in 2D case is proportional to $\propto |\psi_e(x, z)|^2$, so that the subsequent diffusion in the dark proceeds predominantly along the direction of the highest gradient (the growth z direction), making diffusion essentially one dimensional. By contrast, long pumping $T_{\text{Pump}} \geq 0.1$ s in a 2D model makes the polarization profile more isotropic in the xz plane (for an unbounded problem at $T_{\text{Pump}} \rightarrow \infty$ the polarization will tend to a profile with circular contour lines in the xz plane). In other words, after long pumping the system “forgets” the initial profile $\propto |\psi_e(x, z)|^2$ of the QD pumping source. The subsequent diffusion in the absence of pumping (i.e. in the dark) is controlled by the dimensionality of the unpolarized space, and is seen to be faster in the 2D case. From this additional results we conclude that one dimensional model captures the key aspects of QD NSR dynamics, such as slower relaxation following long optical nuclear spin pumping. However, some quantitative discrepancies arise, especially at long T_{Pump} , where dimensionality affects the diffusion dynamics. Such discrepancies are likely to introduce systematic errors in the best fit values of the spin diffusion coefficient D . However, in a real QD system D is not constant, and the approximate nature of the spin diffusion concept itself entails a range of systematic errors. This justifies the use of a simplified one dimensional model to describe our experimental results.

-
- [67] A. Oshiyama and S. Ohnishi, DX center: Crossover of deep and shallow states in Si-doped $\text{Al}_x\text{Ga}_{1-x}\text{As}$, *Phys. Rev. B* **33**, 4320 (1986).
- [68] P. M. Mooney, Deep donor levels (DX centers) in III-V semiconductors, *Journal of Applied Physics* **67**, R1 (1990).
- [69] L. Zhai, M. C. Löbl, G. N. Nguyen, J. Ritzmann, A. Javadi, C. Spinnler, A. D. Wieck, A. Ludwig, and R. J. Warburton, Low-noise GaAs quantum dots for quantum photonics, *Nat. Commun.* **11**, 4745 (2020).
- [70] C. Heyn, A. Stemann, T. Koppen, C. Strelow, T. Kipp, M. Grave, S. Mendach, and W. Hansen, Highly uniform and strain-free GaAs quantum dots fabricated by filling of self-assembled nanoholes, *Appl. Phys. Lett.* **94**, 183113 (2009).
- [71] P. Atkinson, E. Zallo, and O. G. Schmidt, Independent wavelength and density control of uniform GaAs/AlGaAs quantum dots grown by infilling self-assembled nanoholes, *J. Appl. Phys.* **112**, 054303 (2012).
- [72] E. A. Chekhovich, M. M. Glazov, A. B. Krysa, M. Hopkinson, P. Senellart, A. Lemaître, M. S. Skolnick, and A. I. Tartakovskii, Element-sensitive measurement of the hole-nuclear spin interaction in quantum dots, *Nat. Phys.* **9**, 74 (2013).
- [73] E. A. Chekhovich, A. Ulhaq, E. Zallo, F. Ding, O. G. Schmidt, and M. S. Skolnick, Measurement of the spin temperature of optically cooled nuclei and GaAs hyperfine constants in GaAs/AlGaAs quantum

- dots, *Nature Mater.* **16**, 982 (2017).
- [74] Y. Wang and K. Takeda, Speedup of nuclear spin diffusion in hyperpolarized solids, *New Journal of Physics* **23**, 073015 (2021).
- [75] A. Ulhaq, Q. Duan, E. Zallo, F. Ding, O. G. Schmidt, A. I. Tartakovskii, M. S. Skolnick, and E. A. Chekhovich, Vanishing electron g factor and long-lived nuclear spin polarization in weakly strained nanohole-filled GaAs/AlGaAs quantum dots, *Phys. Rev. B* **93**, 165306 (2016).
- [76] D. Huber, B. U. Lehner, D. Csontosová, M. Reindl, S. Schuler, S. F. Covre da Silva, P. Klenovský, and A. Rastelli, Single-particle-picture breakdown in laterally weakly confining GaAs quantum dots, *Phys. Rev. B* **100**, 235425 (2019).
- [77] C. Latta, A. Srivastava, and A. Imamoglu, Hyperfine Interaction-Dominated Dynamics of Nuclear Spins in Self-Assembled InGaAs Quantum Dots, *Phys. Rev. Lett.* **107**, 167401 (2011).
- [78] G. Gillard, I. M. Griffiths, G. Ragunathan, A. Ulhaq, C. McEwan, E. Clarke, and E. A. Chekhovich, Fundamental limits of electron and nuclear spin qubit lifetimes in an isolated self-assembled quantum dot, *npj Quantum Inf.* **7**, 43 (2021).
- [79] E. A. Chekhovich, K. V. Kavokin, J. Puebla, A. B. Krysa, M. Hopkinson, A. D. Andreev, A. M. Sanchez, R. Beanland, M. S. Skolnick, and A. I. Tartakovskii, Structural analysis of strained quantum dots using nuclear magnetic resonance, *Nature Nanotech.* **7**, 646 (2012).
- [80] E. A. Chekhovich, I. M. Griffiths, M. S. Skolnick, H. Huang, S. F. Covre da Silva, X. Yuan, and A. Rastelli, Cross calibration of deformation potentials and gradient-elastic tensors of GaAs using photoluminescence and nuclear magnetic resonance spectroscopy in GaAs/AlGaAs quantum dot structures, *Phys. Rev. B* **97**, 235311 (2018).
- [81] B. Urbaszek, P.-F. Braun, T. Amand, O. Krebs, T. Belhadj, A. Lemaître, P. Voisin, and X. Marie, Efficient dynamical nuclear polarization in quantum dots: Temperature dependence, *Phys. Rev. B* **76**, 201301 (2007).
- [82] R. L. Mieher, Quadrupolar nuclear relaxation in the iii-v compounds, *Phys. Rev.* **125**, 1537 (1962).
- [83] J. A. McNeil and W. G. Clark, Nuclear quadrupolar spin-lattice relaxation in some iii-v compounds, *Phys. Rev. B* **13**, 4705 (1976).
- [84] I. J. Lowe and S. Gade, Density-matrix derivation of the spin-diffusion equation, *Phys. Rev.* **156**, 817 (1967).
- [85] A. G. Redfield and W. N. Yu, Moment-method calculation of magnetization and interspin-energy diffusion, *Phys. Rev.* **169**, 443 (1968).
- [86] A. G. Redfield and W. N. Yu, Moment-method calculation of magnetization and interspin-energy diffusion, *Phys. Rev.* **177**, 1018 (1969).
- [87] E. R. Butkevich and R. K. Sabirov, On anisotropy of nuclear spin-diffusion coefficient, *Physica Status Solidi (b)* **146**, 683 (1988).
- [88] R. K. Harris, E. D. Becker, S. M. Cabral de Menezes, R. Goodfellow, and P. Granger, NMR nomenclature: Nuclear spin properties and conventions for chemical shifts: Iupac recommendations 2001, *Solid*

State Nuclear Magnetic Resonance **22**, 458 (2002)